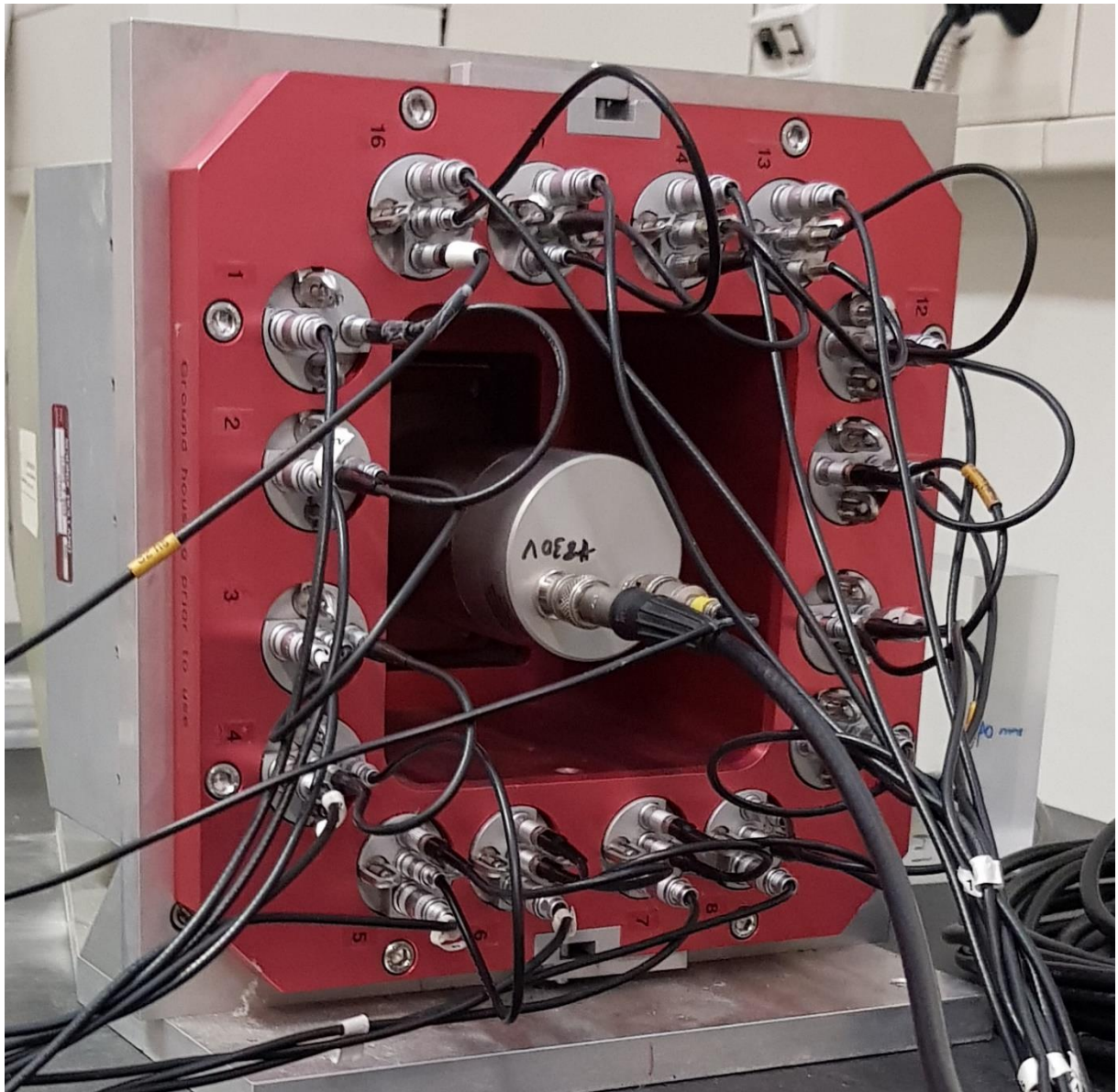# An anti-Compton spectrometer for particle therapy research

Bachelor research project:
Student: Jorn Sangers (S3241513)
Supervisor: Peter Dendooven
Date: 30/05/2019
Physics, University of Groningen

1 Abstract

Gamma rays spectra for several sources, ^{22}Na, ^{24}Na, ^{60}Co ^{137}Cs and ^{241}Am-be have been recorded with an anti-Compton spectrometer (ACS). To determine the system performance in terms of: detection efficiency, resolution and Compton suppression (CSF) at different gamma ray energies. To verify if an ACS would be worth considering for improving the emission spectrum obtained from prompt gammas. Where the prompt gammas are created during irradiation by hardon therapy. Which would allow for real time tracking of the beam range of these therapies. Where this would allow for improving precision of what issue is being irradiated. In this work it was found that the CSF in the Compton regions where of a factor of two up to three for high energy gamma rays.

Table of content

2 Introduction

Hadron therapy is a type of radiation therapy which uses high energy ions, most commonly carbon or protons to irradiate tumours. It can replace the more traditional X-ray based irradiation therapy [1]. As with traditional x rays the energy deposit is over a fairly large area along the path travelled by the particle, figure 3.1. Whereas for high energy ions the dose deposition is very limited and only in a very specific region. The fact that only a small region gets irradiated, makes proton therapy significantly more interesting for cancer treatments. As only the tumour will be irradiate and much more healthy tissue is spared. The reduction in irradiating health tissue makes proton therapy so alluring as it drastically reduces the amount of possible complications compared to traditional therapy. However this high precision comes at a cost, the accuracy of the deposition becomes extremely important.

Currently for particle proton therapy operates with margins of [2-3]% of proton range + [2-3]mm. [2]. Which for deep seated tumours is still fairly inaccurate. The reason as to why this margin is so high is due to the fact that verification of where the proton bundle irradiates inside the body is fairly difficult to determine. The current difficulties and uncertainty in proton range makes it that proton therapy is not used much for radiation therapy near organs or other critical tissues. Which is a loss considering the fact it potentially could spare the health tissue significantly more compared to x-rays.

What has been recently suggested is to use prompt gamma rays emitted by the fission reaction. These gamma rays are immediate immediately upon the fission reaction induced in the cell by the ion beam. It has been demonstrated that by detection of these gamma rays the location of where the radiation hit the patient potentially can be determined in real time[3]. This would allow adjustments in treatment planning and extremely accurate dose delivery.

To accurately determine the energy range from proton beam via prompt gamma rays it is of extreme importance to accurately measure these prompt gamma rays. An obstacle in this is Compton scattering, Compton scattering is an interaction within the detector where the gamma ray loses some of its energy to an electron and the energy will original energy be partially detected. This creates additional background in the spectrum, which is unwanted as it both reduces the resolution as well as in a worst case scenario can obstruct weaker peaks that are present within the spectrum. A possible solution is to employ an anti-Compton shield, a detector around the main detector that is only there to detect radiation scattered by Compton scattering and then via some software tricks reject the belonging count measured in the main detector from the spectrum. The removal of this Compton scattered event will reduce the background which can potentially improve the spectrum as more features will be visible.

In the present work, an anti-Compton spectrometer was used to measure prompt gamma ray energy spectra will be commissioned. Data will be taken with various radioactive sources in various geometries. Data analysis will be done to determine the efficiency, energy resolution and Compton suppression performance of the spectrometer as function of gamma ray energy. In order to verify if an anti-Compton shield principle is indeed enhancing the spectrum obtained for gamma ray detection. Particularly in the high energy region as prompt gammas are primarily high energy gammas[1]

3 Theory

3.1 Radioactivity

Radioactive decay takes place when an unstable atom splits apart via emission of ionizing radiation [4]. The atom wants to reach a lower energy state, it will accomplish this via emission of either alpha, gamma or beta particle. With alpha radiation a helium core splits of the atom. For beta decay either a positron or an electron, depending on whether it's beta plus or minus decay will get emitted and for gamma decay a high energy photon will be emitted.

The frequency at which such an radioactive source emit is known as Becquerel. The activity is then defined as the number of nuclei that undergo transformation during a certain time interval. When the activity is known at a certain time and knowing the half-life the current activity of a source can be determined. This can be calculated via equation 3.1[5]. Where the half-life is defined as the time it takes for when half of the source has radioactively decayed. Each particle will have a unique decay pattern and with that a unique emission spectrum.

$$A(t) = A_0 * e^{-\lambda t} \quad (3.1)$$

$A(t)$: Current activity (s^{-1}), A_0 Acitivty at t_0 (s^{-1}), λ decay constant (s^{-1}) and time passed since t_0 (s)

Where

$$\lambda = \frac{\ln(2)}{t_{\frac{1}{2}}} \quad (3.2)$$

$t_{\frac{1}{2}} = half\ life\ (s)$

3.2 interaction between matter and radiation

As a gamma ray passes through a medium it has a chance to interact with the material. This interaction will result in the gamma ray being absorbed (photo electric effect and pair production) or scatter via Compton scattering[6]. The decrease of intensity of a gamma ray as it travels through a medium can be described by equation 3.3.

$$I(x) = I_0 e^{-\mu_{total} x} \quad (3.3)$$

$I(x)$: intensity at distance x, I_0 incident gamma intensity and x is the distance traveld in the material

Where

$$\mu_{total} = \mu_{photo\ eletric} + \mu_{compton\ scattering} + \mu_{pair\ production} \quad (3.4)$$

Is the total absorption coefficient as a sum of the attenuation coefficients from each possible interaction with matter.

The absorption coefficient is dependent on the incident gamma ray. Where depending on the energy each different interaction becomes more or less likely. In figure 3.1 Each of the μ values dependence on energy is displayed. The next section will explain exactly the nature of these interactions with matter. Which results in 3 regions each dominated by a different interaction.
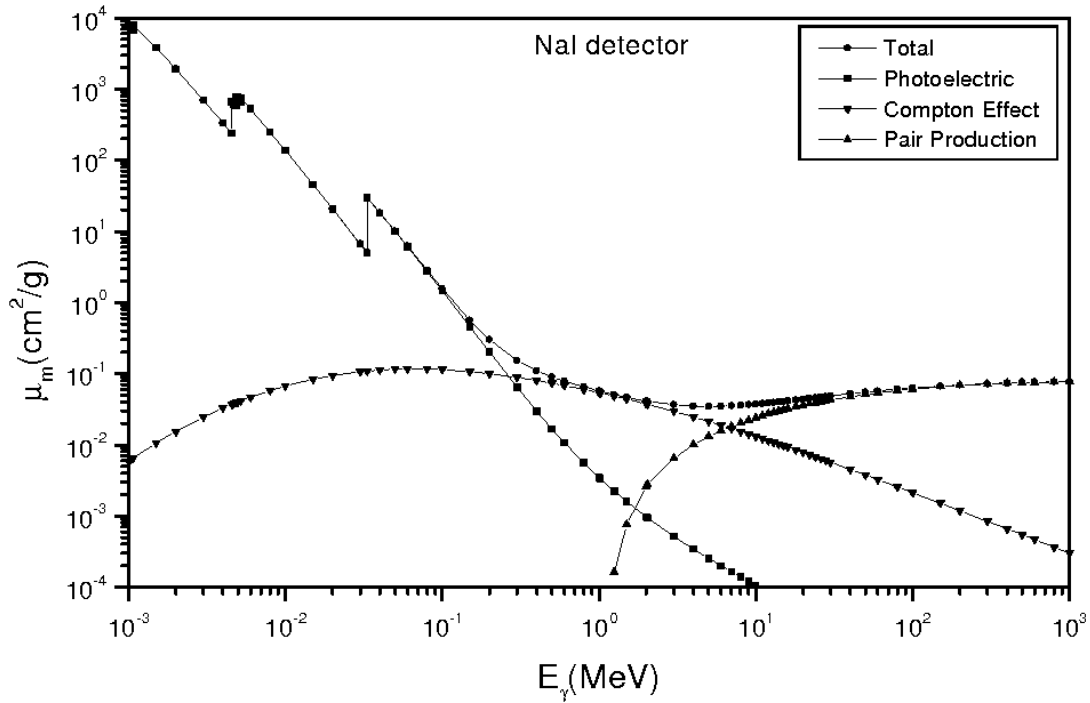
Figure 3.1 all μ values from formula 3.4 for different gamma ray energies for an NaI detector [7]

3.2.1 Photo electric effect

In the photoelectric absorption process a photon disappears completely as it absorbed by an absorber atom[8]. This energy will be absorbed to an outgoing electron[9]. The energy of that outgoing electron will be equal to binding energy subtracted from the gamma ray energy, formula 3.5.

$$E_{e^-} = hv - E_b \ (3.5)$$

$h \ is \ the \ Plank's \ constant, v \ is \ frequency \ of \ the \ photon \ and \ E_b \ is \ the \ binding \ energy \ of \ the \ electron$

The vacancy resulting from the ejection of the electron is filled up through either capturing an electron from the surrounding or rearrangement of the electron for another shell in the atom. As a result one or multiple characteristic x-ray have a chance to be emitted.

From equation 3.5 it can be determined that the energy is proportional to the incident gamma energy. Furthermore from figure 3.1 it can be observed that The photo electric effect is dominant in the low energy region.

3.2.2 Compton scattering

The second type of interaction that gamma rays can have with matter is Compton scattering. Instead of the photon being fully absorbed the photon will scatter on an electron. The electron will then partially absorb the energy of the photon and both the electron and photon will be scattered as a result. The process of Compton scattering can be seen in figure 3.2 [10]. The scattering results in the photon being deflected with an angle θ. Which in turn determines the change in energy for the photon as per equation 3.6 [11].

Compton scattering is thus an form of inelastic scattering, where the energy of the photon changes. It dominates the interaction between few 100 keV up until a few MeV.
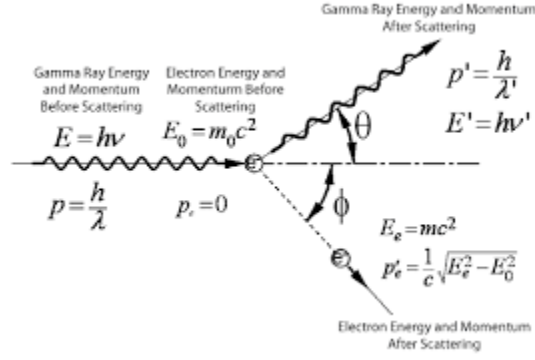
Figure 3.2: Compton scattering, A schematic overview of the process.

$$E' = \frac{E_0}{1 + \dfrac{E_0}{m_0 c^2}(1 - \cos(\theta))} \quad (3.6)$$

E' energy of photon after collision, E_0 energy of the incident gamma, m_0 restmass of electon, c speed of light and θ s

3.2.3 Pair-production

The last type of interaction a photon can have is pair-production. Pair-production is the physical process where the incident gamma ray, splits up in a position and an pair-production interaction can occur when the energy of the incident gamma ray is greater than 1.022 MeV. This energy corresponds the twice the rest mass of electrons ($m_0 c^2$ =5.11 keV for electrons [11]). The remaining energy will be split, that is the incident gamma ray energy not used towards pair production, will be transformed into kinetic energy for the electron and position in a random 20-80% split between them [11]. A minor part of the energy will also be absorbed by the nucleus.

The positron, after slowing down, will annihilate with an electron and transform into a two photons of 511 keV. Pair-Production becomes important at higher energies, starting roughly at the 2 MeV mark. When a

3.3 Scintillation detectors

Scintillation detectors are detectors capable of detecting gamma rays. It does so by converting the high energy photons into visible photons. The light yield from these photons proportional to the energy of the original gamma ray. These visible photons can then be detected by a light sensitive detector[13] after they have been enhance in a Photomultiplier tube (PMT). A schematic of an scintillation detector can be found in figure 3.3:
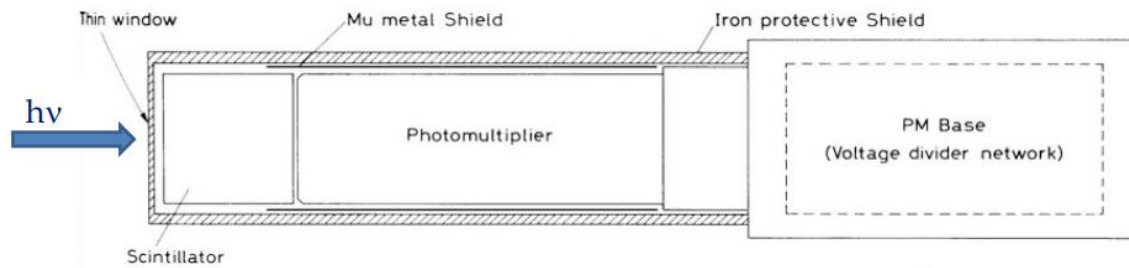

Figure 3.3: Schematic of a scintillation detector[12]

3.3.1 Inorganic scintillators crystals

The scintillation process for inorganic materials depends on the energy states. These energies are determined by the lattice of the material [14]. In the discrete energy bands for semiconductor or insulators, there exists valance and conduction band. Where the conductions band are the electrons that can freely move in the crystal and the valance are bound to the bound electrons. Intermediate between these energy bands is the forbidden bad where electrons cannot be found.

The detectable photon is created when by excitation the electron moves from the valance band to the conduction band. The excitation happens when the photon is absorbed by the photoelectric effect and the energy is transferred to the electron. Which results in a hole in the valance band, where normally an electron would be. Then when the electron de-excites and falls back to the valance band to it emits a photon. This photon can be in the visible energy range and be detectable.
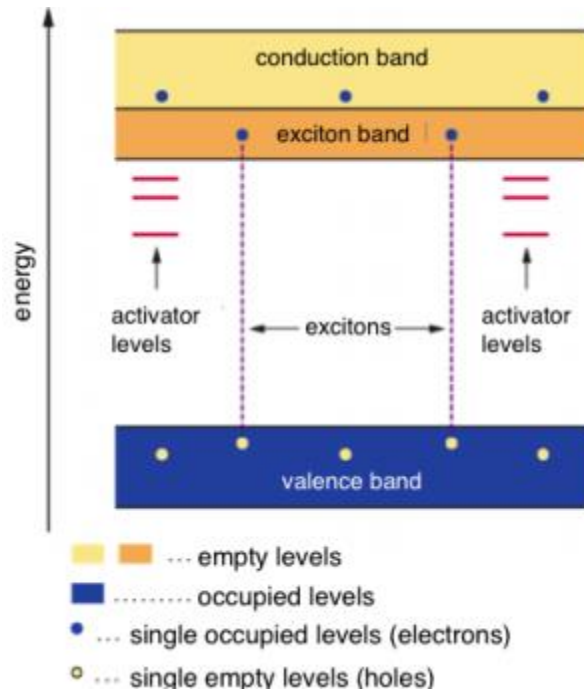

Figure 3.4 Electron band principle for Inorganic scintillators [15]

However this process is inefficient and often won't produce a photon in the visible range. Thus impurities are added, in the case of NaI, this will be Thallium. These activators will introduce addition energy sites [13, 14, 15]. The energy band structure with activators can be seen in figure 3.4[15]. These activator sites enhance probability of the emission of a visible photon. These additional energy levels reduce the width between energy states, which reduces the energy transition width. This reduction in width between energy states is responsible will increase the likelihood of a visible photon to be emitted.

3.3.2 Photomultiplier tube (PMT)

The signal obtained from the scintillation process is very weak and needs to be amplified before detection can take place. A PMT is a device which allows for this amplification needed. The photo-cathode convers the incoming gamma ray photon from the crystal into a electrons. In figure 3.5 such a schematic for a PMT can be seen. A high negative voltage is applied to the photo-cathode [16]. This voltage will then be divided between the dynodes. The reaction that result is called the electron multiplication reaction. Here the electron will accelerate due to potential difference between the cathode and the first dynode. Once the electron has accelerated and hit the first Dynode it will generate a few additional electrons. The original and generated electrons will then accelerate due to the potential difference between the first and second dynode. Again upon interaction each of these electrons will generate a few (3 to 4) electrons each. This then is the multiplication process as each time each of the generated electrons will produce these extra electrons at the next dynode. The multiplication process repeats until the end of the PMT where, the signal output is collected. Typical photodetector consist of 9 to twelve of such dynodes[16].
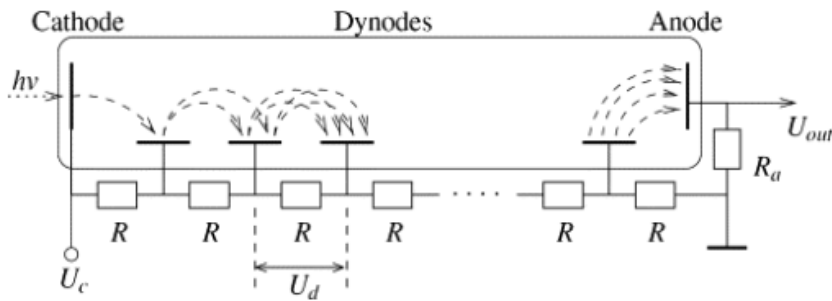

Figure 3.5: Working of a Photomultiplier Tube (PMT) [16]

3.4 Categorization of Scintillation detectors

What is obtained from the detector is called an energy spectrum. Where the amount of counts in an volt binned in channels) is shown. An example of such a spectrum can be seen in figure 3.6 [17]. The spectrum for a single energy peak exist of 2 major regions. The photopeak, where the full energy of the peak is absorbed and the Compton region where not all of the initial gamma ray energy will be detected. The Compton regions exist of three sub regions. The Compton edge, where the angle between the photon and electron is 180 degrees, which is the maximum value, note formula 3.6. The Compton plateau where the angle between the gamma ray and photon can have any value. Finally the backscatter peak where the scatting of 180 degrees has taken place outside of the detector.
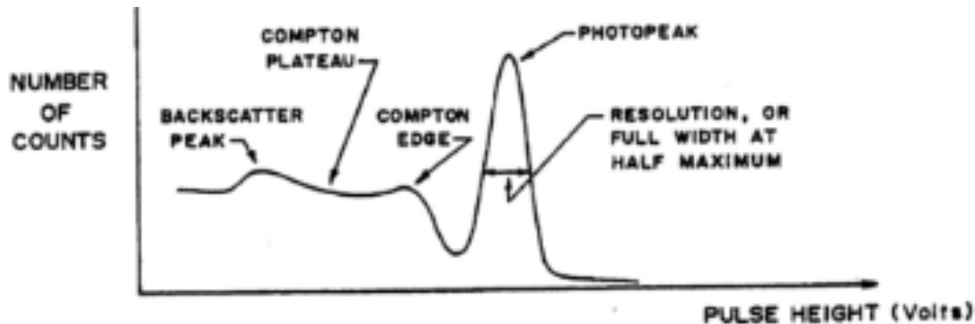

Figure 3.6: Typical spectrum of radioactive source [17]

3.4.1 Energy calibration

The Energy calibration entails transforming the channels into energy. This can be achieved by locating position of the energy peak in the spectrum and plotting this against the value for the peak energy[14]. The value for peak energy is known for each source as each isotope emits their own unique gamma ray energy, or combination of gamma emission energies. These values for the peaks where obtained from sources [19] and [20].
After calibration is properly executed, the resulting spectrum is an energy versus count spectrum.

3.4.2 Energy resolution

Energy resolution is of the detector can be derived from formula 3.7[14]. Where the FWHM is the full width half maximum of the photopeak (Figure 3.6). The resolution is a measure for broad the peak is, with smaller values being more desired. The lower the R value the more one accurate the photopeak position can be determined and be distinguished. This becomes more in more important gap in energy between photopeak's becomes smaller, here detectors with a low value for R will be able to distinguish between the two, whereas for high R value detector will show it as one peak, due overlap. The energy resolution has, when the setup is optimized, a typical value for an certain energy depending on the crystal material.

$$Energy\ resolution[R] = \frac{FWHM}{Photo\ Peak\ energy}\ (3.7)$$

3.4.3 Peak efficiency

As described by beer's law there exists a chance for interaction between the gamma ray the scintillation crystal. Because of this not all gamma rays will interact with the detector [14]. This makes it useful to quantify the detection efficiency. In the present work we are interested in detecting gamma rays in the photopeak. So the efficiency of the detector will be defined by equation 3.8. The efficiency is described by the counts measured in photopeak versus how many the source has sent out. Where the activity is the amount of decays are happening on average per second. The branching ratio is the, chance of a given photopeak to be emitted from that decay.

$$\text{Efficiency} = \frac{Count\ measured\ in\ a\ photopeak}{Activity\ of\ the\ source * branching\ ratio * measurement\ time}\ (3.8)$$

3.4.4 Anti Compton performance

The Anti Compton performance is described the Compton suppression factor (CSF)[18]. The CSF is defined by equation 3.9. Where the Compton supressed spectrum is generated from imposing a filtering condition on the energy spectrum. This condition is: If the Shield detects a gamma ray within a short time window, the count will be rejected and not be taken account into the spectrum. The logic behind is that, when a gamma ray is detected in the shield this means that this gamma ray has undergone Compton scattering. Which means that the gamma ray that was simultaneously detected in the main detector has reduced energy and would only contribute to the background of the spectrum. Here the higher the CSF the more Compton scattered events are rejected and background is reduced.

$$CSF(E) = \frac{counts\ for\ a\ certain\ energy\ in\ unaltered\ energy\ spectrum}{counts\ for\ a\ certain\ energy\ in\ compton\ suppressed\ spectrum}\ (3.9)$$

4 Experimental setup

4.1 The sources

The source activity is calculated with equation [3.1] using the original value and date provided by the supplier of the source. In the measurements the activity of the sources will be reflected in measurement duration, with weaker sources taking up more time. These sources have been chosen as they represent a wide array of energy peaks ranging from 511keV to 4.4MeV. This allows for a more accurate and broader determination of the effects of an anti-Compton spectrometer.

Source	Current Activity (Bq)
^{137}Cs	1,75E+05
$^{241}Am\text{-}Be$	3,44E+09
$^{60}Co\ (1)$	5,13E+03
$^{60}Co\ (2)$	3,40E+03
^{22}Na	1,91E+05
^{24}Na	Unknown

Source	Current Activity (Bq)
137Cs	1,75E+05
241Am-Be	3,44E+09
60Co (1)	5,13E+03
60Co (2)	3,40E+03
22Na	1,91E+05
24Na	Unkown

Table 4.1 Activity of the used sources

4.2 The Setup

The Energy spectra for the sources mentioned in table 4.1 was measured via the setup in figure 4.1. With as goal to characterise the anti-Compton spectrometer, in terms of energy/channel, peak resolution, detection efficiency and anti-Compton performance at different energies. The difference in energy coming from these difference sources from table 4.1. The measuring tape on the side was to ensure the source was at the correct distance. A lead wall was put in place to shield the operator from unnecessary radiation from the radioactive sources. Next to the lead wall, for [241]Am-Be measurement a Boron-loaded wall was placed to protect against the neutrons emitted by this source. For similar safety reasons regarding radiation for the operator.
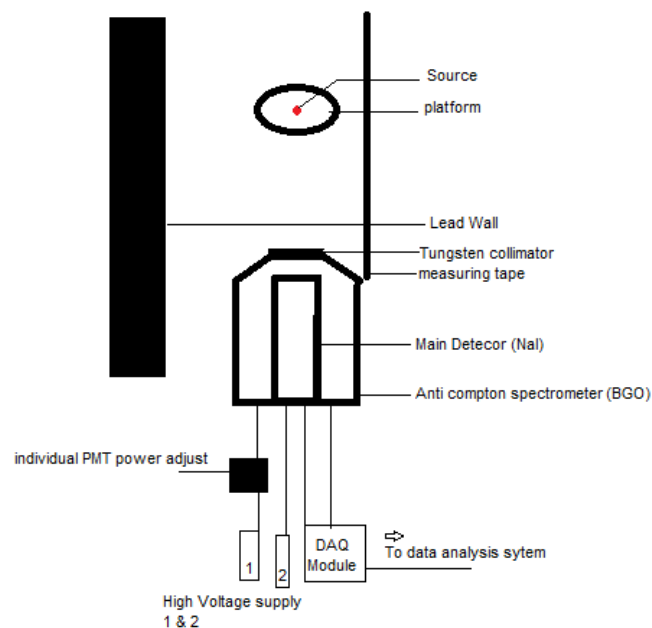

Figure 4.1 Schematic of the setup

4.2.1 Main NaI detector

The main and middle detector used as a Sodium iodine (NaI) scintillation crystal. The dimensions can be found in appendix X.X. NaI is one of the most common scintillation detector materials due to its high light yield. Here NaI is used due to its common use in detectors and its respectable energy resolution. The detector is supplied by a single high voltage supply with a value of 830Volt.

4.2.2 The anti-Compton shield.

The anti-Compton shield is a devise that surrounds the main detector and is a scintillation detector made from BGO. In front of the detector, a tungsten collimator is installed such that the source will not directly irradiate the detector. The detector consisted of multiple segments each with their individual PMT and power cable. Via a shared power supply split by the individual PMT high voltage adjuster. The proper calibration is necessary to reduce peak broadening and unnecessary loss of energy resolution. Detailed data regarding the detector can be found in appendix [9.1-2]. Although BGO has poorer energy resolution compared to NaI, it has a high absorption rate making it very suitable for an anti-Compton spectrometer.

4.2.3 The DAQ module

A 16-channel digital pulse processing module which has been developed to be suitable for a wide range of radiation detectors and to deliver high resolution in energy and time measurement was used. It is responsible for reading in and pre-processing the signals obtained from the detector. Furthermore it handles the digitalization of the data. It does so by creating an event, which consist of a time- and amplitude timestamp. Figure 4.2 contains a schematic of the module
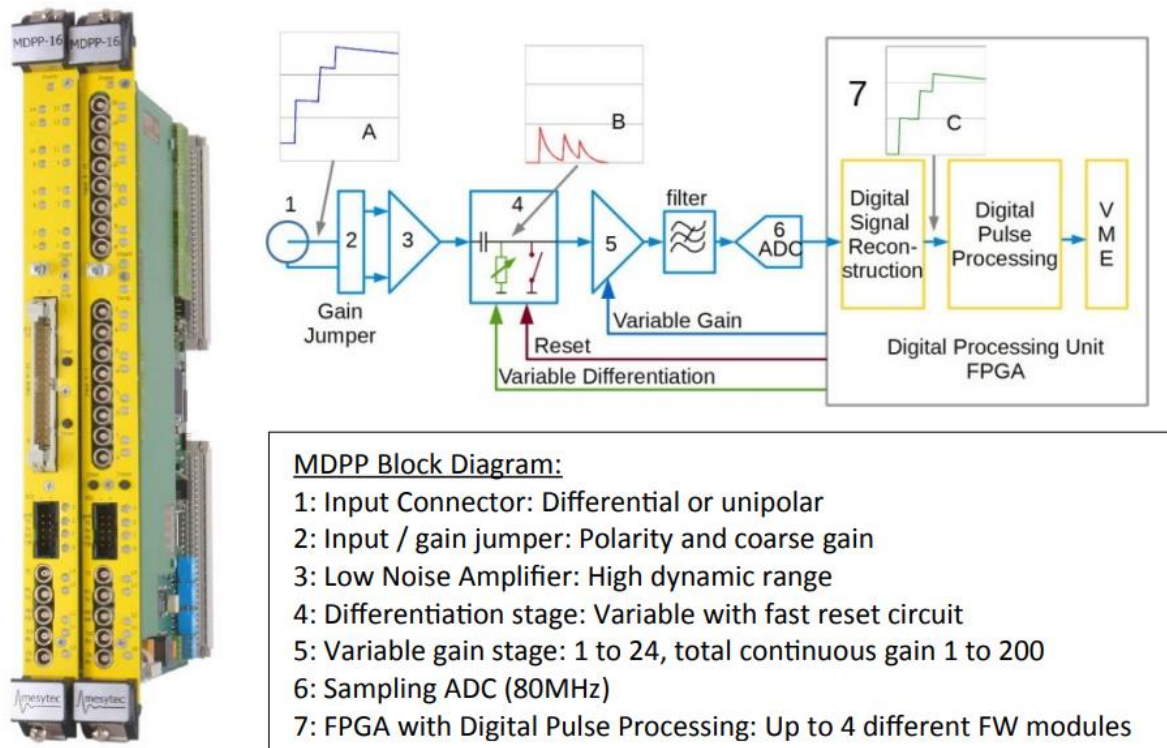

Figure 4.2 MVME data-acquisition module [21].

4.3 The Setup Calibration and measurements

4.3.1 PMT high voltage adjustment

The first step was to adjust the high voltage delivery to each of the BGO detectors. Each detector needed to have the peak in the same position in the energy spectrum. For this calibration, the source was placed inside the detector. Then the spectra of two individual detector units were calibrated to have their peak at equal position. This step is fairly important to prevent unnecessary peak broadening. For this measurement the source wasn't placed as in figure 4.1, but put inside the detector, to allow for proper calibration of the BGO shield.

4.3.2 Settings calibration

The second step was optimizing the energy resolution. This involved tweaking the settings of `settings for signal processing for the detector. By iterating over many settings and comparing the FWHM/Peak ratio of the measured spectra, the best performing setting were chosen. For these calibrations, a 22Na source was used as the high activity and presence of two peaks allowed for more accurate calibration. The settings found to be optimal are shown in table 4.2. Similar to section 4.2.1 these setup measurements the source was placed in the detector.

4.3.3 Measurements

Finally the measurements were taken where the source on the platform at a distance. The source was placed at 158 and 250mm away from the detector. These distances were chosen because 158mm was the focal point of the detector system and 250mm is a relevant distance for possible applications of the system. The source was placed on a heightened platform to bring the source on the same height as the centre of the detector. The measuring tape on the side was to ensure the source was at the correct distance. A lead wall was put in place to shield the operator from unnecessary radiation from the radioactive sources. For the ^{60}Co measurement, both sources were used at the same time due to the low remaining activity of the sources due to their age. Finally, next to the lead wall, Boron-loaded plates were placed to protect against the neutrons emitted by the ^{241}Am-Be

Setting	Value (BGO)	Value NaI
threshold	0x00FF	0x00FF
PZ	0x0010	0x0010
tf_int_diff	100	30
gain	1322	1115
shaping_time	100	30
BLR	2	2
reset_time	30	30
signal_rise_time	40	38

Table 4.2 Optimal data acquisition settings found for the detectors

4.4 The software

To accommodate the measurements, two software packages where used: "mvme - VME DAQ" was used to drive the data acquisition module described in 4.2.3. and "IGOR PRO", a data analysis program that allows for more advanced calculations of the recorded spectra.

4.4.1 DAQ program

The program is responsible for interacting with the DAQ module and recording the data obtained from the detector. The first window from the left in figure 4.3 holds the controls of recording, how the data should be stored and the settings of the module. A fragment of the module settings can be seen in the second window. Here one can adjust the settings to the behaviour of the module to attain optimal peak resolution. The third window is contains the preliminary data-analysis. In the current setup, 3 types of graphs are made: 1D energy spectra of counts/channel for each detector, 2D energy spectra of the BGO and NaI detector and 1D (anti-)coincidence spectrum of the detectors. The (anti-)coincidence spectrum was made via a conditional filter where if the BGO detector measured something in coincide with the NaI detector the datapoint would get either rejected or accepted.

The DAQ program also allowed for energy calibration. However, this was found to be insufficient and was one of the reasons to IGOR PRO software program. The final screen demonstrates the output of one of the graphs, where the energy spectrum can be observed. The program is able to fit the peak with a gaussian curve. This functionality was used to optimize the settings to obtain best energy resolution. However, due to the limitation of not accounting for background, this limitation was another reason to employ the use a second program which allowed for better data analysis.
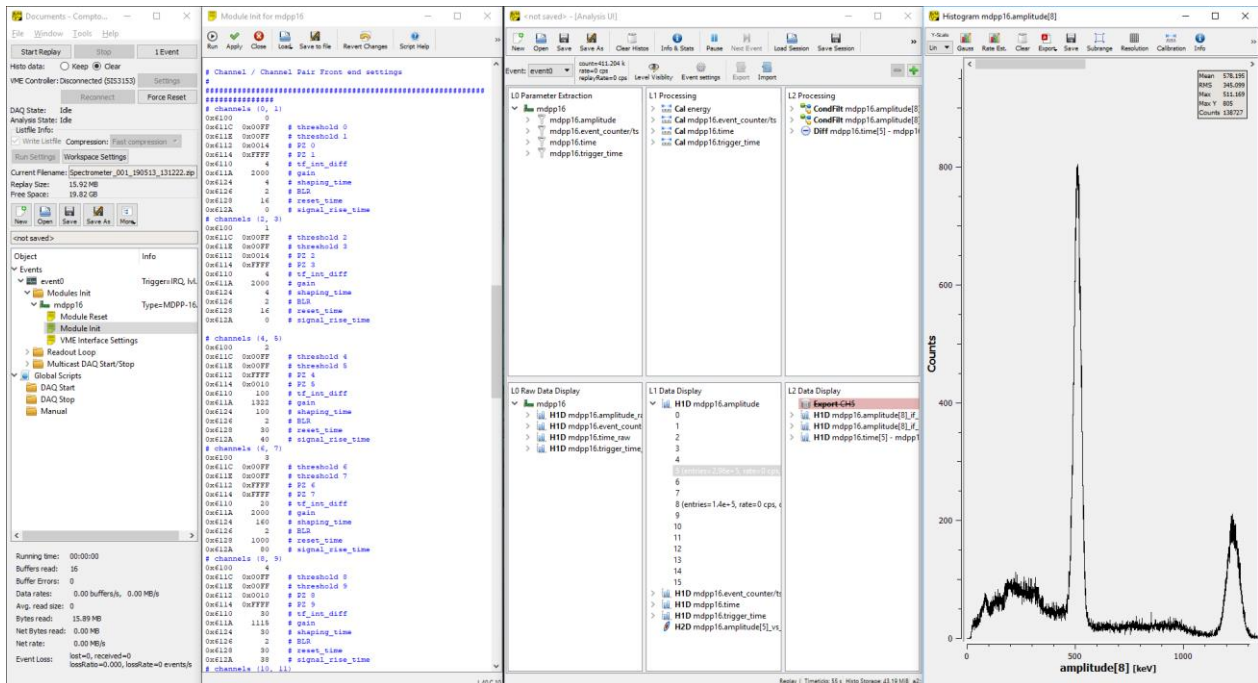

Figure 4.3 MVME data-acquisition software.

4.4.1 Data analysis Program

IGOR pro was used to analyse the data and process the results obtained by the detector through the DAQ system. First the 1D data from the histograms produced by the DAQ program are read. The data is then plotted in an XY diagram. The X axis was based on the energy calibration curve found by plotting the gamma ray energy of the peaks versus the spectrum channel number. This energy calibration made peaks appear at their energy value rather than channel number, which carries actual physical meaning. Then via 'compress waves' the value of 16 channels was merged into one, which reduces statistical fluctuations and smoothens out the curve. The typical look of the program can be seen in figure 4.3. From left to right: A data browser, the compressed spectrum (top) and the uncompressed spectrum (bottom), the gaus-lin fit function creation window (top) and the compressed wave window (bottom)

Once the data was properly calibrated, peak analysis was done. Firstly via the gauss-lin function. Which is a function of a gaussian curve with a linear background. The values found for FWHM and peak position were used for calibration and data recorded in the present work.

$$f(x) = \left(w_3 + w_4 * (x - w_0) + 0.9395 * \frac{w_1}{w_2} * exp\left(-2.773 * \left(\frac{x - w_0}{w_2}\right)^2\right)\right)(4.1)$$

w_0 = centre of gaussian w_1= area of gaussian w_2= FWHM of gaussian w_3 = constant of background w_4 = slope of background

The area of the peak was determined by w_1 of formula 4.1 . This was done to determine peak efficiency and peak/total ratio needed for assessing the Compton improvement.
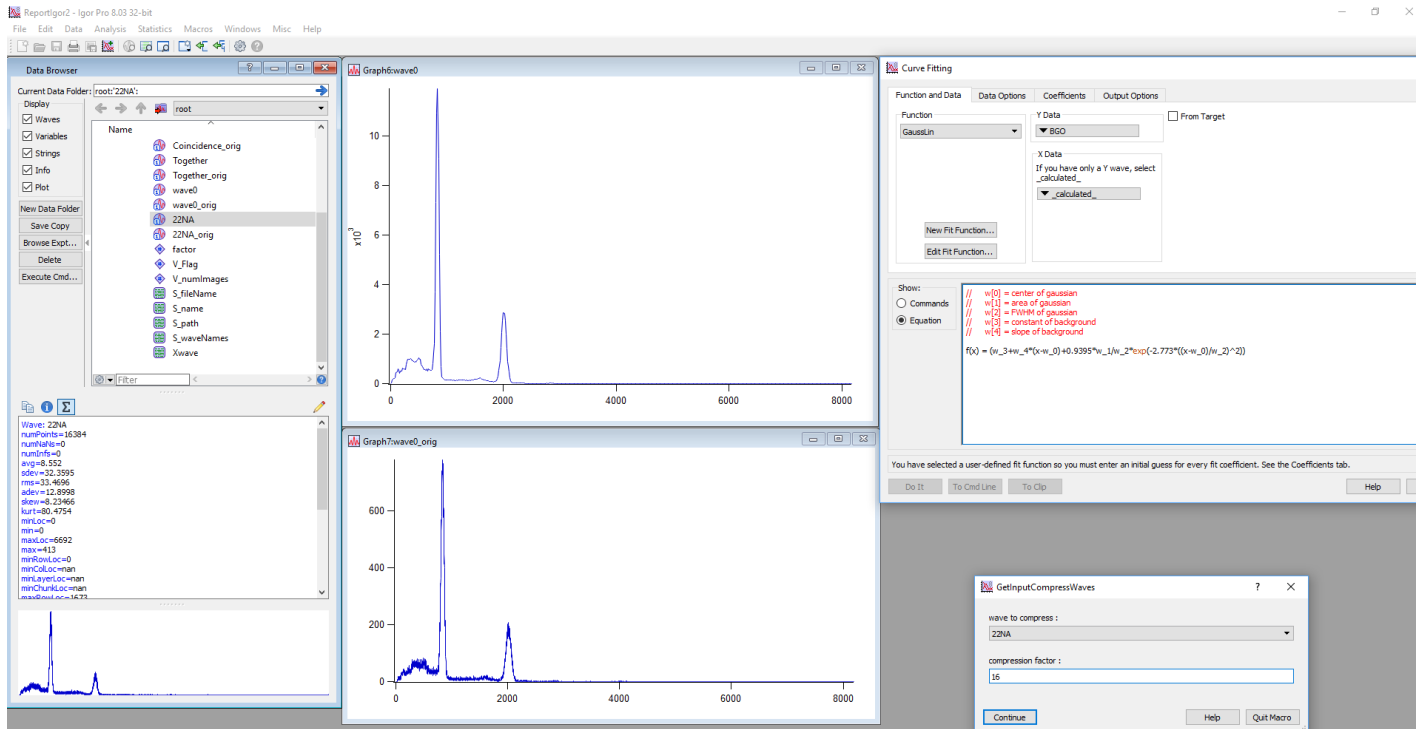

Figure 4.3 Igor Pro, a data analysis software package

5 Results

5.1 Energy calibration

The peak energy as described in section 3.4.1 was used for the sources ^{22}Na ^{60}Co and ^{137}Cs. Then a second calibration was made for ^{24}Na, consisting of the peaks from ^{24}Na, ^{40}K and ^{232}Th, the latter two of the peaks coming from background radiation rather than a source. The last calibration for ^{241}Am-Be was done with its peak and first escape peak. By plotting this energy versus the channel number in which the peak was determined to be, the energy calibration was determined. The curve, a linear fit, found after plotting energy versus channel, has a slope and an offset, with the slope being equal to the energy per channel. The calibrations were different between these measurements as settings of the data-acquisition system had changed leading to varying energy per channel values.
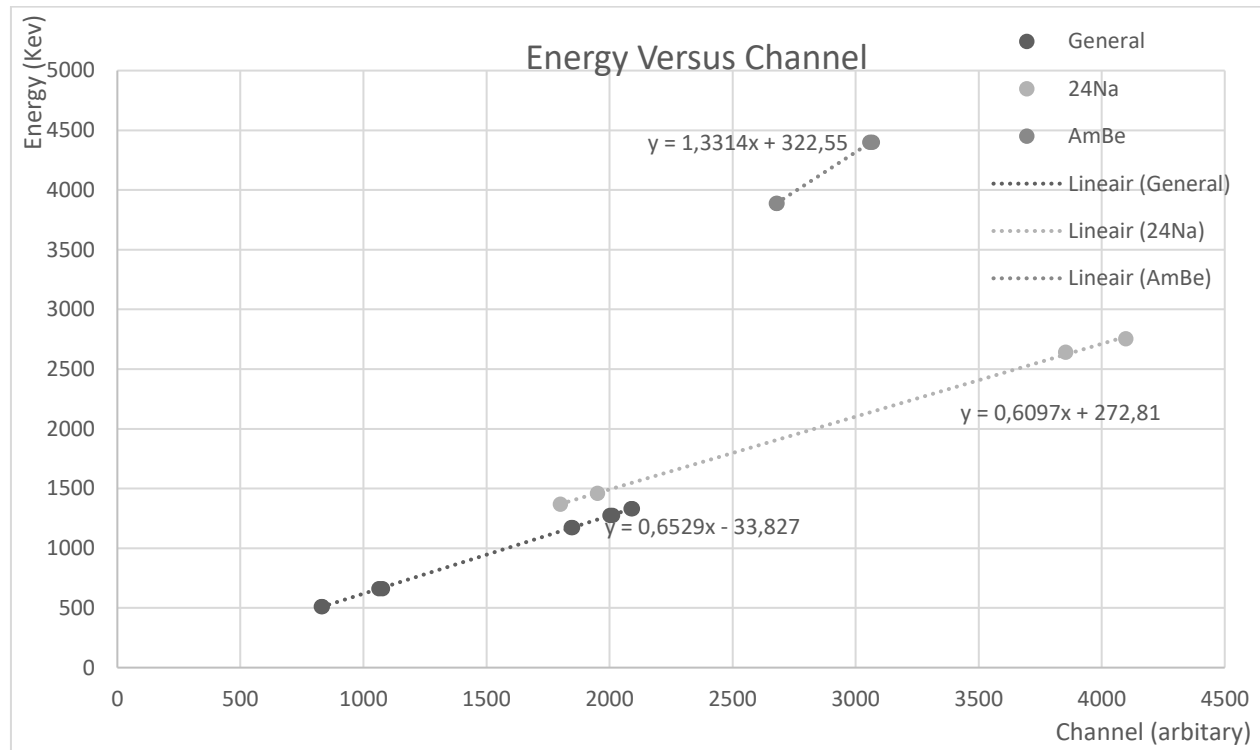
Figure 5.1. Energy calibration of the NaI detector, general include the sources: ^{22}Na ^{60}Co and ^{137}C

5.2 Energy Resolution

The energy resolution of the NaI detector has been determined via the FWHM. The result is figure 5.2 where FWHM/peak energy is plotted against peak energy. The measured points are from the ^{22}Na, ^{24}Na, ^{60}Co, ^{137}Cs, ^{40}K and ^{232}Th peaks. The light grey coloured measured points are from the ^{241}Am-Be source. These point were excluded as another factor, called doppler broadening affected these points.

The FWHM has been determined via the FWHM of gaussian fit with a linear background in the IGOR. The energy resolution is found to be decreasing as the energy increases. The curve is similar to other works [22] as it is typical of a NaI detector. What can be observed is a curve with the function of $0,8122x^{-0,372}$.
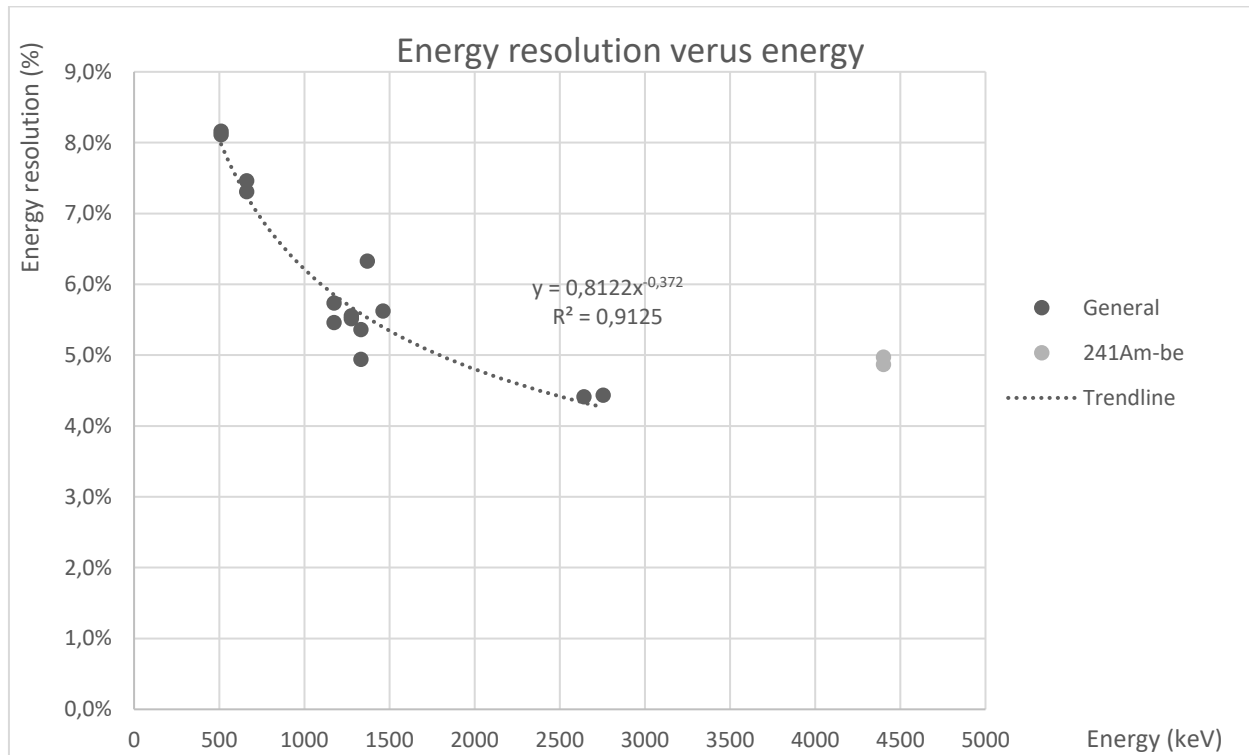
Figure 5.2 Energy resolution versus peak energy

5.3 The energy spectra
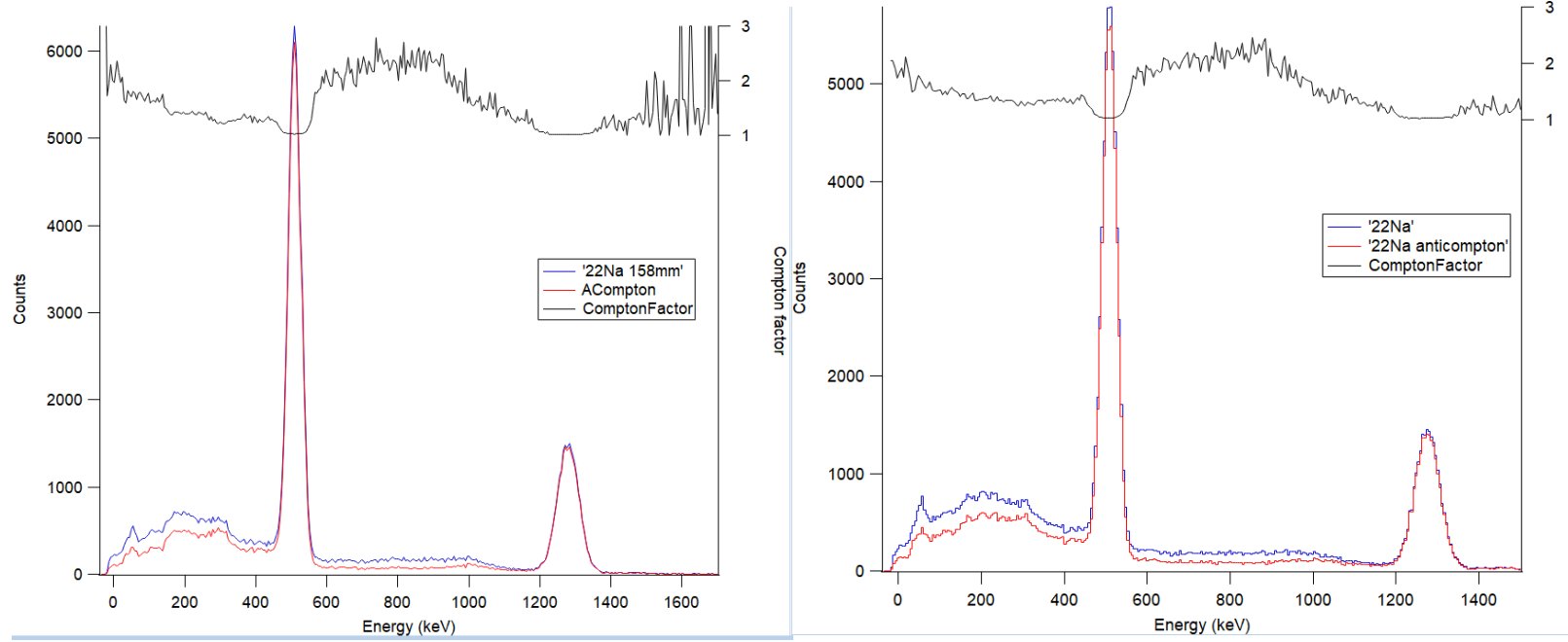
Figure 5.3 The energy spectrum, anti-Compton spectrum and Figure 5.4 Compton suppression factor with the ^{22}Na source at 155 (left) and 250mm (right)
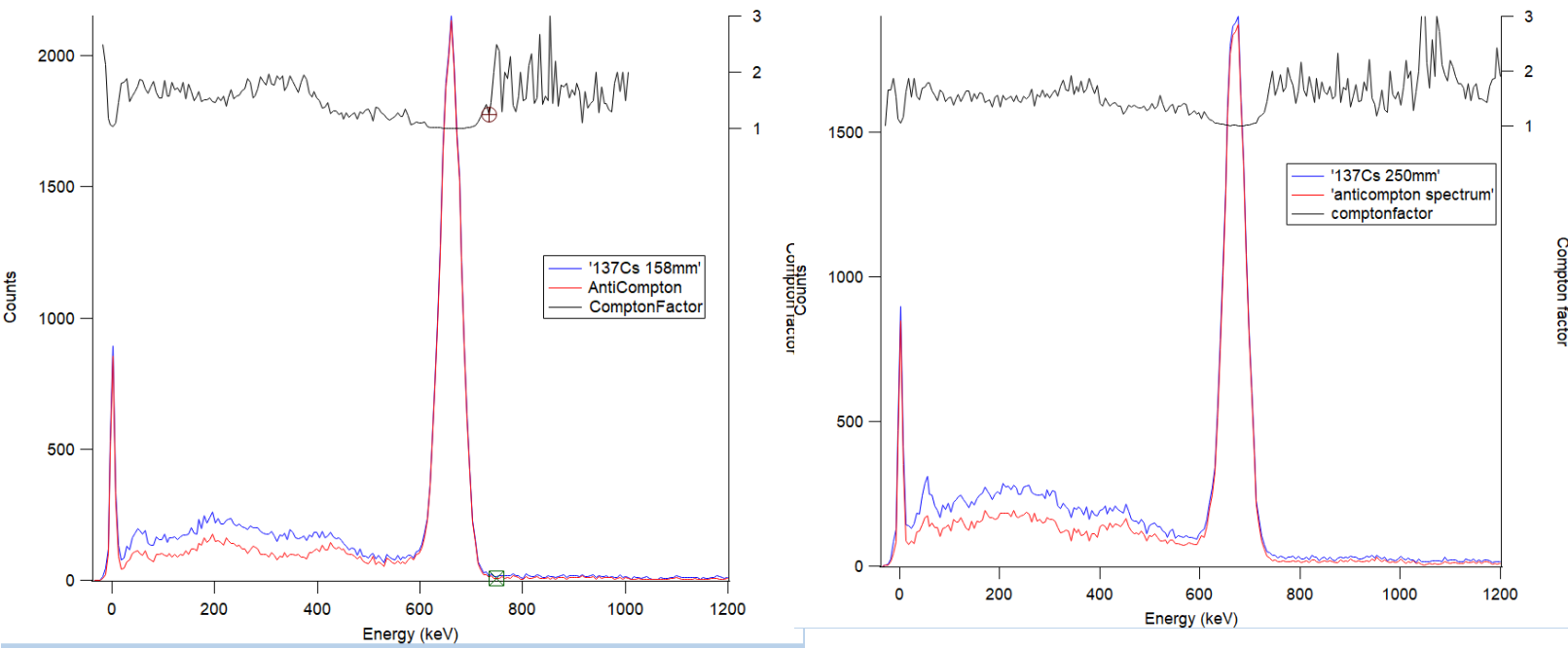
Figure 5.5 The energy spectrum, anti-Compton spectrum and Figure 5.6 Compton suppression factor with the ^{137}Cs source at 158mm (left) and 250mm (right)
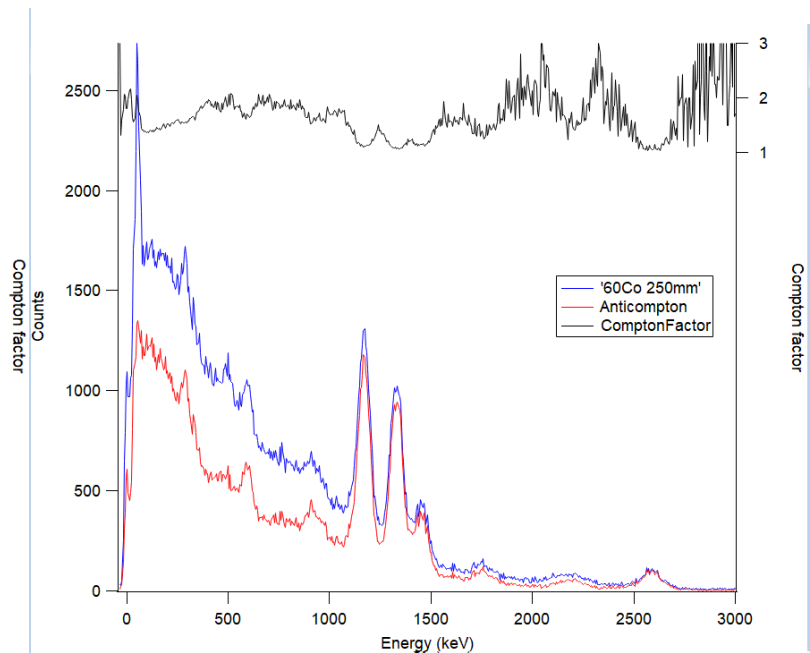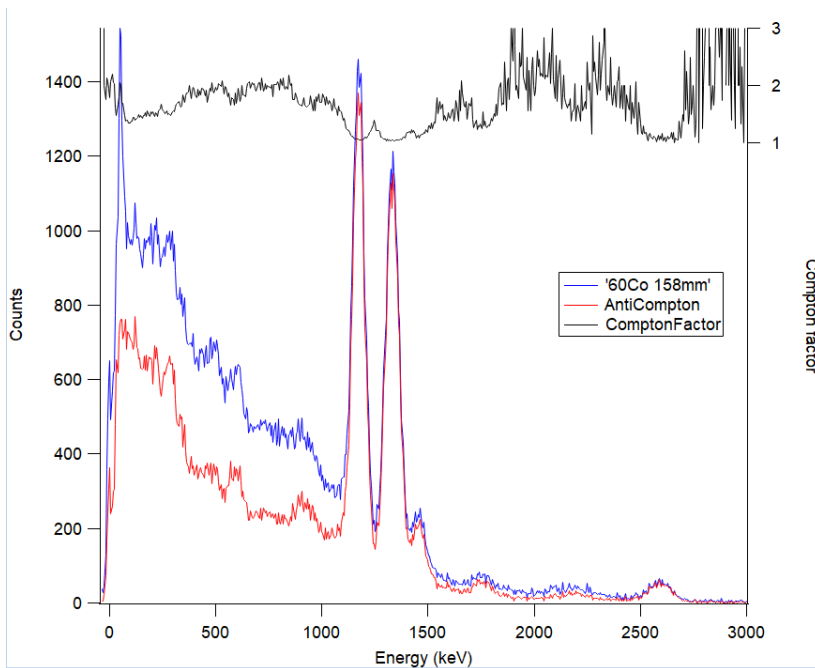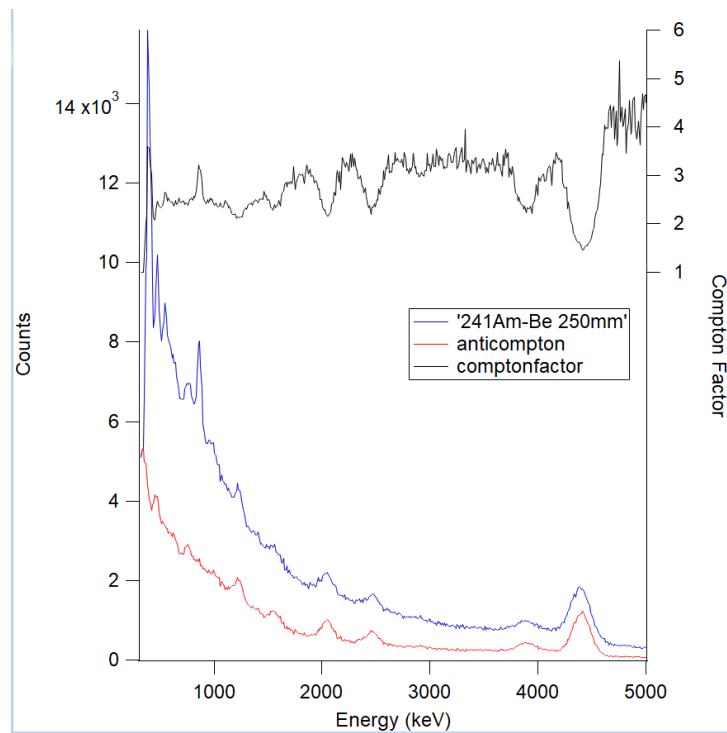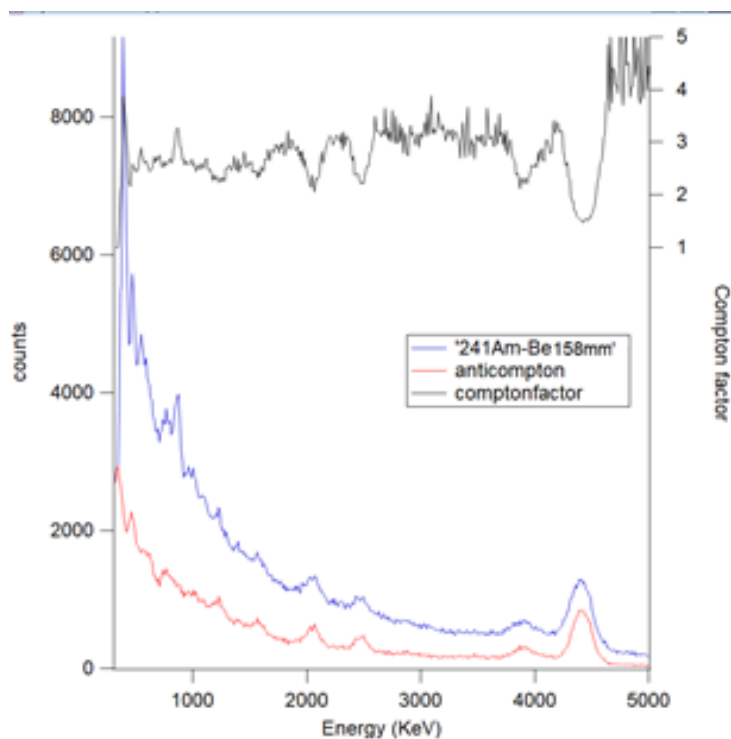
Figure 5.7 The emission spectrum, anti-Compton spectrum and Figure 5.8 Compton suppression factor with the ^{60}Co source at 158mm (left) and 250mm (right)

Figure 5.9: The emission spectrum, anti-Compton spectrum and Figure 5.9 Compton suppression factor with the ^{241}Am-Be source at 158mm (left) and 250mm (right)
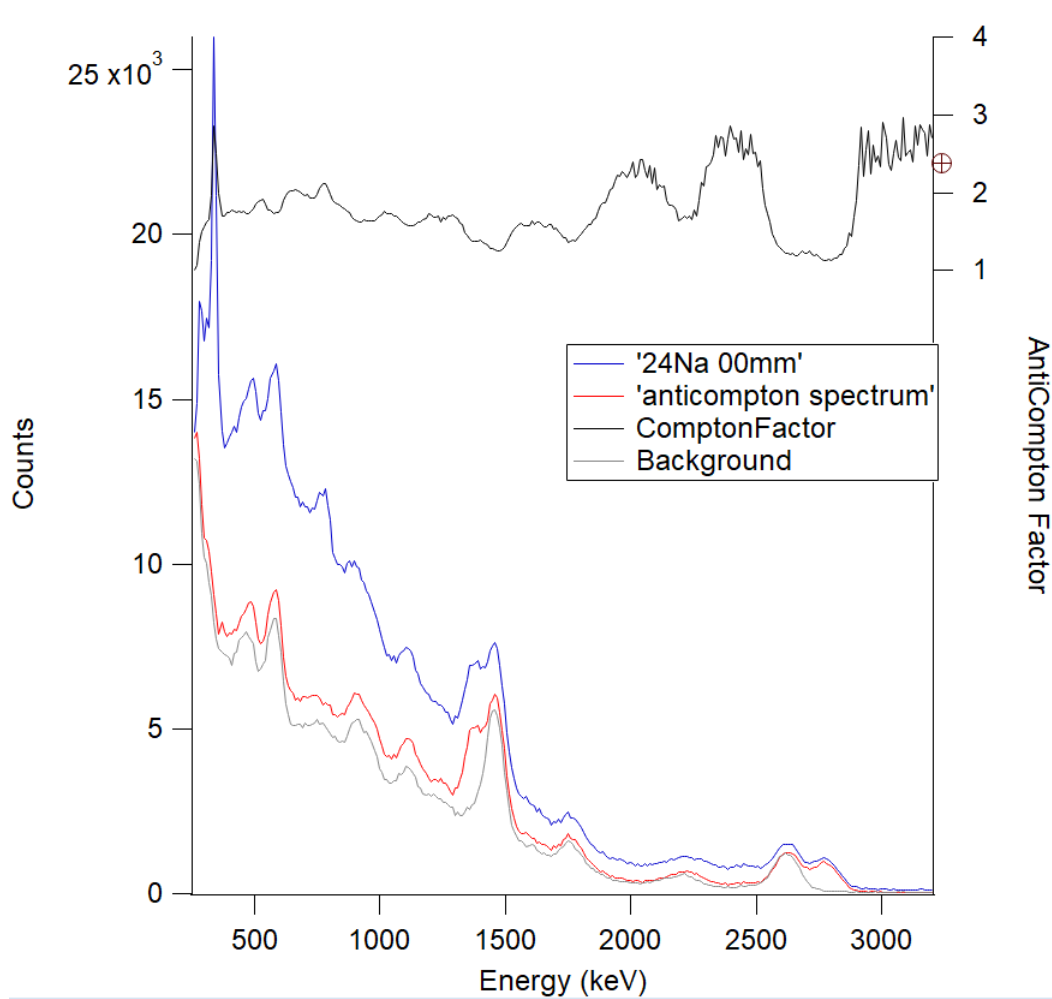
Figure 5.10 The emission spectrum, anti-Compton (background) spectrum and Compton suppression factor with the ^{24}Na source at 0mm from the detector

5.4 2D peak analysis

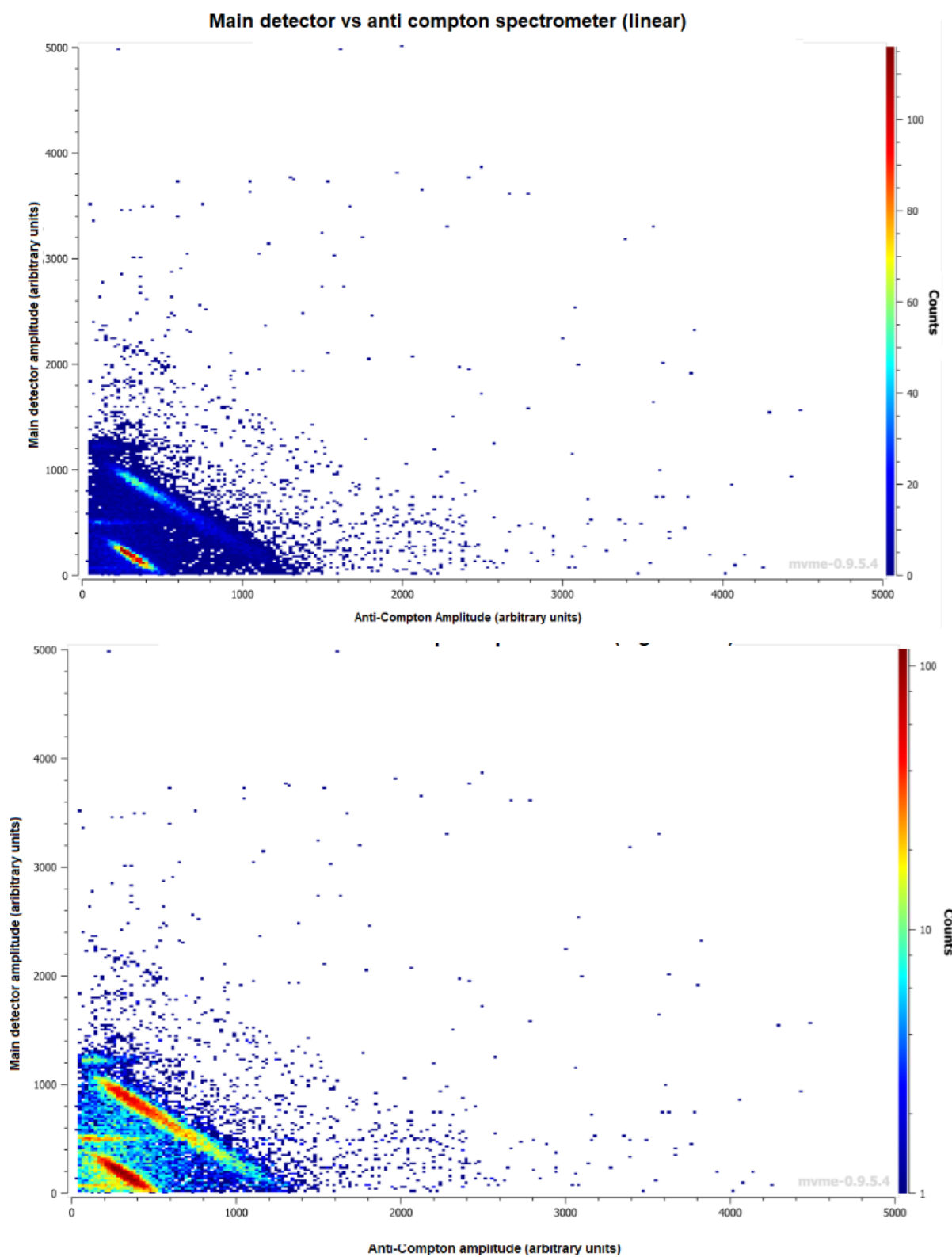**Main detector vs anti compton spectrometer (linear)**

Figure 5.11 2D energy spectra of main vs Compton detector with a ^{22}Na source, linear scaling on the top 5.11a and 5.11b with a logarithmic scale

From the picture two major band can be observed. These bands are the regions where the sum of the energy is equal to 511 and 1275 keV. As these are the peak regions, they contain more counts, as a result these areas will be more intense. This is confirmed by the graph and can be observed in figure 5.11 as these bands. In both graphs, but more explicitly the logarithmic one, Two more regions with increased count rate overlap can be observed. These are the two straight lines around 500 and 1200 on the y axis. These regions correspond to a pure peak is measure simultaneously with background from the environment. What is also be observed, primarily with the logarithmic scale, are two horizontal lines. These correspond to the 511 and 1275keV peaks fully absorbed in the NaI detector while in the BGO an unrelated gamma ray is detected. A possible origin of these unrelated gamma rays is that it's the detection of a Compton scattered gamma ray of either the 511 or 1275keV peaks unrelated to the original. The other 2D spectra can be found in Appendix 9.3.

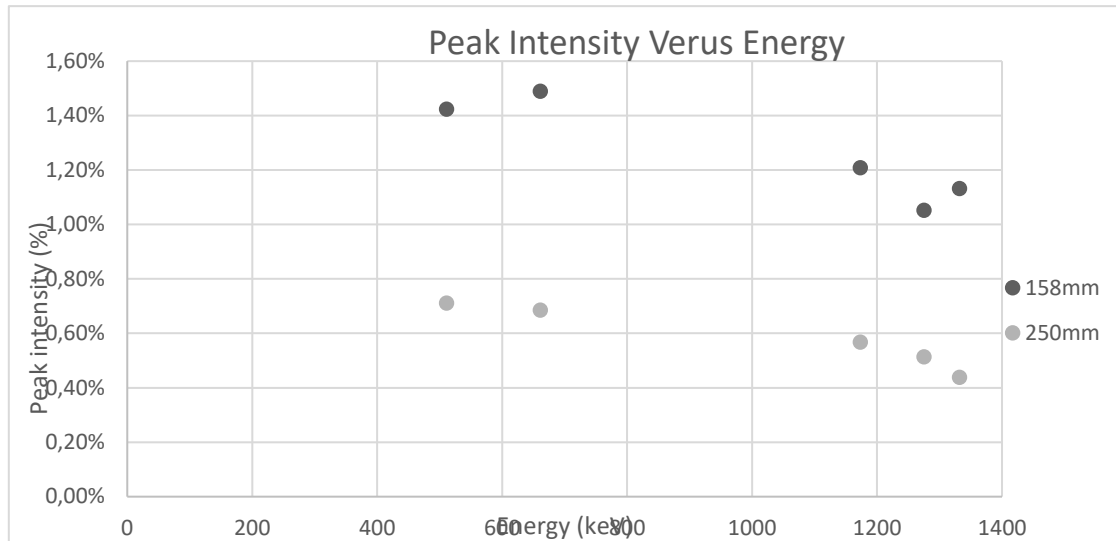## 5.5 Peak efficiency of the spectra:

Figure 5.11 Peak efficiency

After Analysis of the spectrum shown in figure 5.3 to 5.10 the data gave rise to the values found in table 5.1. Peak energy has been determined by the IGOR, gaus-lin as mentioned in section 4.3. Similarly the FWHM has been determined with IGOR. The energy resolution has been determined with equation [3.7]. What can be observed is that as energy goes higher the detection efficiency becomes worse. Furthermore a difference between the two distances can be observed. The cure of 250mm is sleeper and is lower. This is due to geometrical effects, where less radiation will reach the detector. The energy efficiency is what is expected based on extrapolation of previous works[22]. It's important to note that for determination of the energy resolution, the background (grey line in figure 5.10) was removed. As removing the overlap between the ^{24}Na and ^{40}k and ^{232}Th peaks increased the accuracy of determining both the FWHM and peak positions.

Source	Distance	peak (channel)	E peak Literature (keV)	FWHM (keV)	Energy resolution	Activity (Bq)	Branching ratio	Measurement duration (s)	Peak efficiency
^{232}Th	0	3853	2614	116	4.4%	Unknown	-	2905	-
^{24}Na	0	1800	1369	87	6.3%	Unknown	0,9999	2905	-
^{24}Na	0	4097	2754	122	4.4%	Unknown	0,99855	2905	-
^{40}K	0	1950	1461	82	5.6%	Unknown	-	2905	-
^{137}Cs	158	1063	661	48	7.3%	1,75E+05	0,851	47	1,49%
^{22}Na	158	832	511	42	8.2%	1,91E+05	1,78	55	1,42%
^{22}Na	158	2012	1275	71	5.6%	1,91E+05	0,994	55	1,05%
^{60}Co	158	1849	1173	64	5.5%	8,53E+03	0,9985	795	1,21%
^{60}Co	158	2093	1332	71	5.4%	8,53E+03	0,999826	795	1,16%
^{137}Cs	250	1077	661	49	7.5%	1,75E+05	0,851	96	1,37%
^{22}Na	250	828	511	41	8.1%	1,91E+05	1,78	55	1,31%
^{22}Na	250	2002	1275	70	5.5%	1,91E+05	0,994	55	1,01%
^{60}Co	250	1844	1173	67	5.7%	8,53E+03	0,9985	1446	1,05%
^{60}Co	250	2088	1332	66	4.9%	8,53E+03	0,999826	1446	0,80%
^{241}Am-be	158	3067	4400	219	5.0%	3,44E+09	-	490	
^{241}Am-be	250	3057,3	4400	214	5.9%	3,44E+09	-	915	

Table 5.1 measurement data for the different sources

5.5 Anti Compton performance

The Anti Compton performance can be seen in figure 5.3, where the black line represents the Compton suppression factor (CSF). The CSF is defined by equation 3.1. What can be observed is a ratio of 1 around each of the peak regions, meaning that the Anti-Compton spectrometer does not impact these areas just as it should. Furthermore, an upwards trend can be observed, whereas the energy increases the CSF does so too. This indicates that the effectiveness of an Anti-Compton Spectrometer becomes more and more valuable as the energy of the gamma ray increases.

6 Discussion

6.1 Energy Calibration curve

In this work the energy calibration had to be split up into 3 curves (figure 5.1). Ideally this should not be the case and one calibration for all measurements is preferred. However, circumstances did not allow for this to happen. ^{24}Na had to be separated due to the fact that the peaks did not fit on the curve with the others. What exactly caused this shift to happen is unknown, as the settings of the DAQ model had not been changed. To calibrate ^{24}Na better, background gamma rays were taken into account for calibration. As this measurement lasted significantly longer due to the very low activity of the source, enough data was obtained to calibrate with background peaks of ^{40}K and ^{232}Th. However, it is the only measurement which was performed after changing the original settings for gain for the ^{241}Am-be measurement. This might have caused the parameters to be exactly the same, even if this settings was set back to be the to the previous non ^{241}Am-Be measurements.

The ^{241}Am-Be measurement, as mentioned, had different setting for gain compared to the other measurements. The gain was changed, due to an unfortunate discovery that the last 7000 channels (out of 64K) did not record any data, due to thus far unknown reasons. For ^{241}Am-Be, a less favourable method needed to be used. This method has some reductions in quality as it uses the first escape peak. This peak is generally known and can be observed in the data of section 5.4 to have a less well-shaped peak, reducing the accuracy, which has especially more impact considering only two points which are relatively close in energy where used for the calibration. Most notable from these calibrations is the fact that ^{24}Na and ^{241}Am-Be had a large offset, regardless the impact of this will be minimal for the energy resolution and CSF. A plausible explanation could be fluctuations in the PMT, but the exact cause is unknown. Or as ^{24}Na had a vastly different count rate, which could have caused this shift in energies.

6.2 Energy resolution curve

In the energy resolution (figure 5.2), the energy of ^{241}Am-Be was left out because it falls out of the expected trajectory. A likely explanation lies in the fact that the 4.4MeV peak created by the excited carbon is affected by Doppler broadening as found in. Doppler broadening causes an extra uncertainty in peak energy and thus affects the energy resolution. Which makes the value not relevant for determining the intrinsic energy resolution. Hence this measurement wasn't taken into account.

Another feature of note was ^{24}Na, ^{40}K and ^{232}Th resolutions being slightly off their predicted value, most notably the value for the 1369 keV peak of ^{24}Na. There are two possible causes for this: first, as mentioned earlier, the system behaved differently as even though settings were exact replicas the gain was changed. Perhaps possible fluctuations in the High voltage supply, might have caused both this broadening and the change in energy peak in 6.1 . The second and more probable explanation is the interference of the background spectrum. The 1369 and 2754 keV peaks are extremely close to 1461 and the 2614 keV, the overlap might have caused a reduction in accuracy as it was hard to determine which count came from this peak. The background was removed (grey line in figure 5.10) from the spectrum ^{24}Na, however due to the random nature of gamma ray detection, this method is imperfect as background will not be similar. As a result of this spread an R^2 of 0,911, with a function of was determined $0,812x^{-0,372}$, which is slightly off the 1 over square root predicted. If however these sources are excluded a fit of y = $1,451x^{-0,46}$ with a R^2 = 0,9756 which is a lot closer to the predicted values. Furthermore the fit is much better, which confirms that something was different about the sodium 24 measurement.

6.3 Peak Efficiency

The obtained the obtained efficiency vs. gamma ray energy curve was as expected (figure 5.5). Although the data had a fairly large spread, the overall trendline is what is expected: decreasing efficiency for higher energy and distances. The spread is a result from the uncertainty in the peak counts. As was found when computing this value, the error was quite large for some of the spectra measured, leading to a larger spread. Furthermore, as the source distance is of importance here, it is important to note that the [241]Am-Be source location was unknown as it was located somewhere in a tube. Therefore it was assumed that it was in the centre middle, which might lead to a few centimetres off for the distance. The efficiency versus distance scales as 1/distance^2 the difference with an presumed uncertainty of 2cm. Then for the 158mm it could have affected the efficiency by a factor of 1.31x, which is still on the acceptable end.

[241]Am-Be and [24]Na had to be excluded due to one of the variables not being available. For [24]Na, the activity was not available as the source was only locally created and with no equipment present to measure the activity. Therefore, the activity is unknown and the efficiency cannot be determined.

6.4 Compton suppression factor

What can be observed is that the Compton factor is increasing as energy increases (figures 5.3-10) This is as expected as more radiation will escape the central NaI detector at higher energies, causing more radiation to be detected in the anti-Compton spectrum. The CSF had values anywhere between one in the peaks to four in the high energy regions and values of minimally two in the non-peak regions. So an antioption spectrometer is beneficial at all energies in Compton reduction and increasingly so at higher energies.

6.5 General notes and improvements

The best solution to counter the issue mentioned in 6.1 is to measure 1 type of source but with different activity, to inspect the influence of count rate upon peak position. Doing this for several sources with different peak energies should give some insight in this strange behaviour of the detector. Another option would be to variate the distance more as the detection rate decreases as the source moves further away. The distance method however seems like the less inaccurate method between the two mentioned here. As the influence of geometric effects will also play a role in those measurements.

To more precisely determine the energy resolution and calibration, additional sources should be used. Specifically sources with energy peaks around between 1400 and 2700 keV and sources past 4.4MeV. This would allow for more detailed energy calibration, determination of energy resolution and relative peak efficiency .

In this experiment a new type of data-acquisition was used. To be able to characterize the measurement apparatus more, it would be advised to perform additional measurements. Several particularities of the apparatus found during working with the module were: Measuring data in all (even when not connected to a detector) channels when the room lighting is switched on. To prevent this from having an influence, the lights where kept on at any time during a measurements. Another option would be, as this wasn't the case in the setup used in the current work, to properly shield the data-acquisition module. Between channels 1 and 4, an unwanted link between the channels was observed as for these channels, inputting signal from one of the detectors resulted in a significant amount of counts being observed in

one of these neighbouring channels. To prevent this from influencing, channel 5 and 8 where used where this behaviour was found to be absent. However, complete exclusion of any effects from this is not guaranteed.

As the module was used for the first time, it had to be properly configured. Although settings configuration has been rigorously optimized. This was accomplished by via iterating over a large amount of settings combinations and choosing the optimal parameters each time. There still remains a possibility that these settings where not the most optimal. Resulting in a decreased energy resolution as was the case for the 7.82% for the 511keV of ^{22}Na. This peak was slightly above literature values [6] and indicates that the setup has not been as optimized as it could be, however well within the typical range.

As a final note, in the setup used in the present work, the gain matching for the PMT of the individual modules of the anti-Compton spectrometer proved to be vital, as small inaccuracies between the gain of each module caused significant peak broadening. However, before each measurement the setup was checked with a control measurement and compare data, to prevent this from happening.

7 Conclusion

In this work the anti-Compton performance, energy resolution and peak efficiency have been analysed for several sources: ^{22}Na, ^{24}Na, ^{137}CS, ^{60}Co and ^{241}Am-Be.

With a Compton background reduction of 2 to 4 times depending on energy, the Anti-Compton spectrometer was proven to be effective thus worth to consider implementing into research, especially above an energy of 3 MeV where the effectiveness was found to be the highest. Proving that has established an anti-Compton spectrometer for detecting radiation from particle therapy.

Appendix

9.1 The NaI detecor
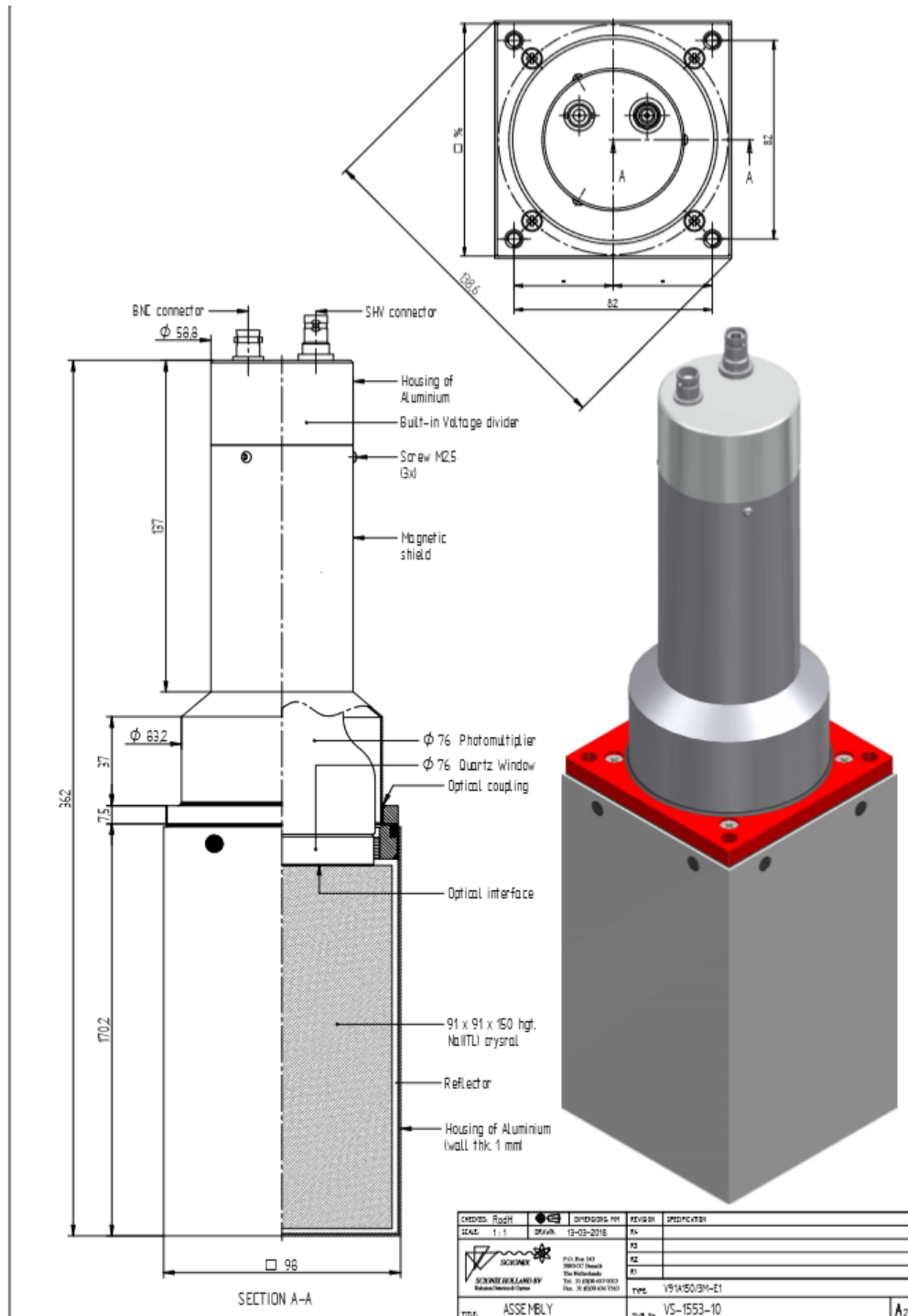
9.2 BGO, Anti Compton shield/spectrometer.
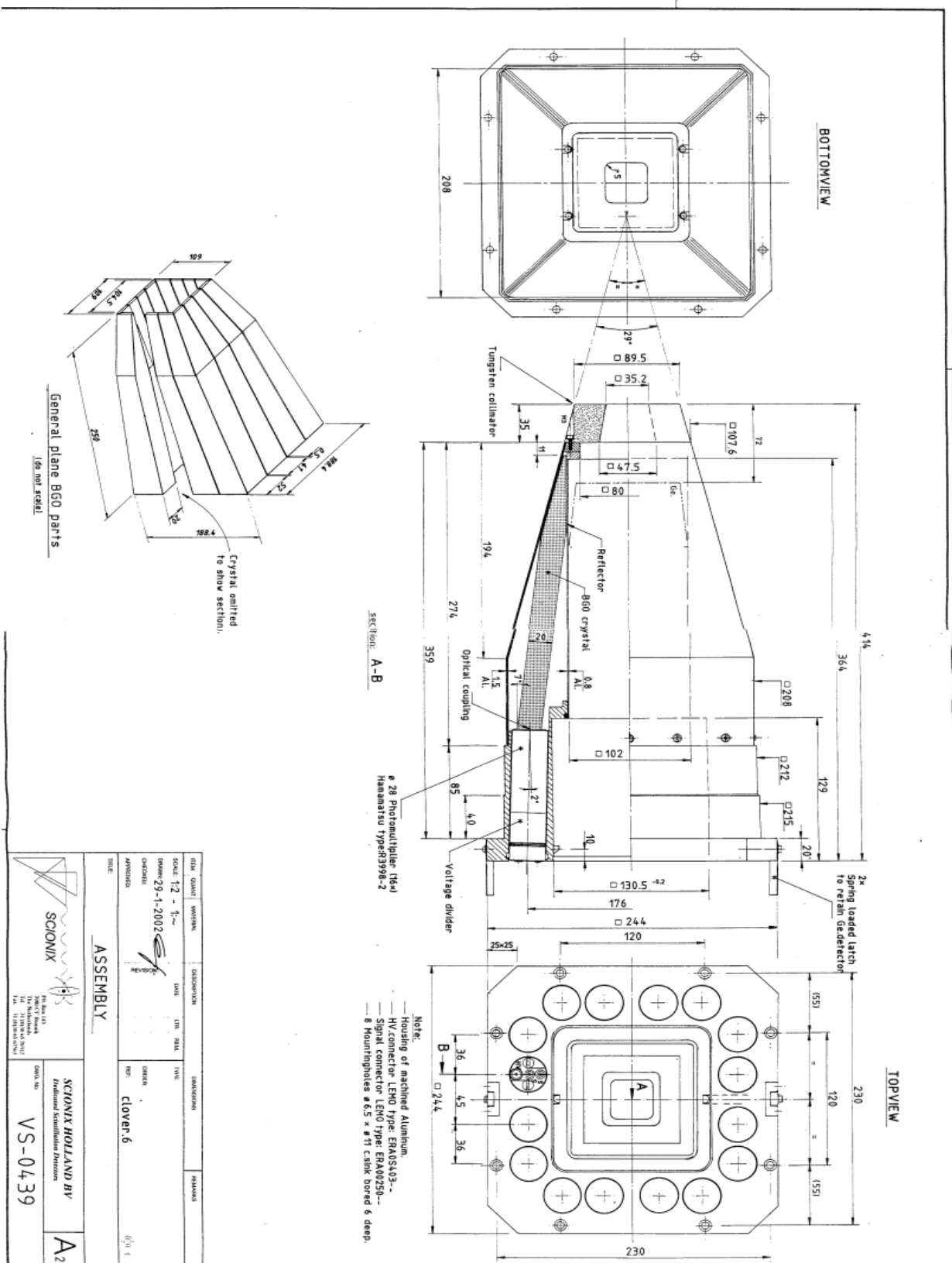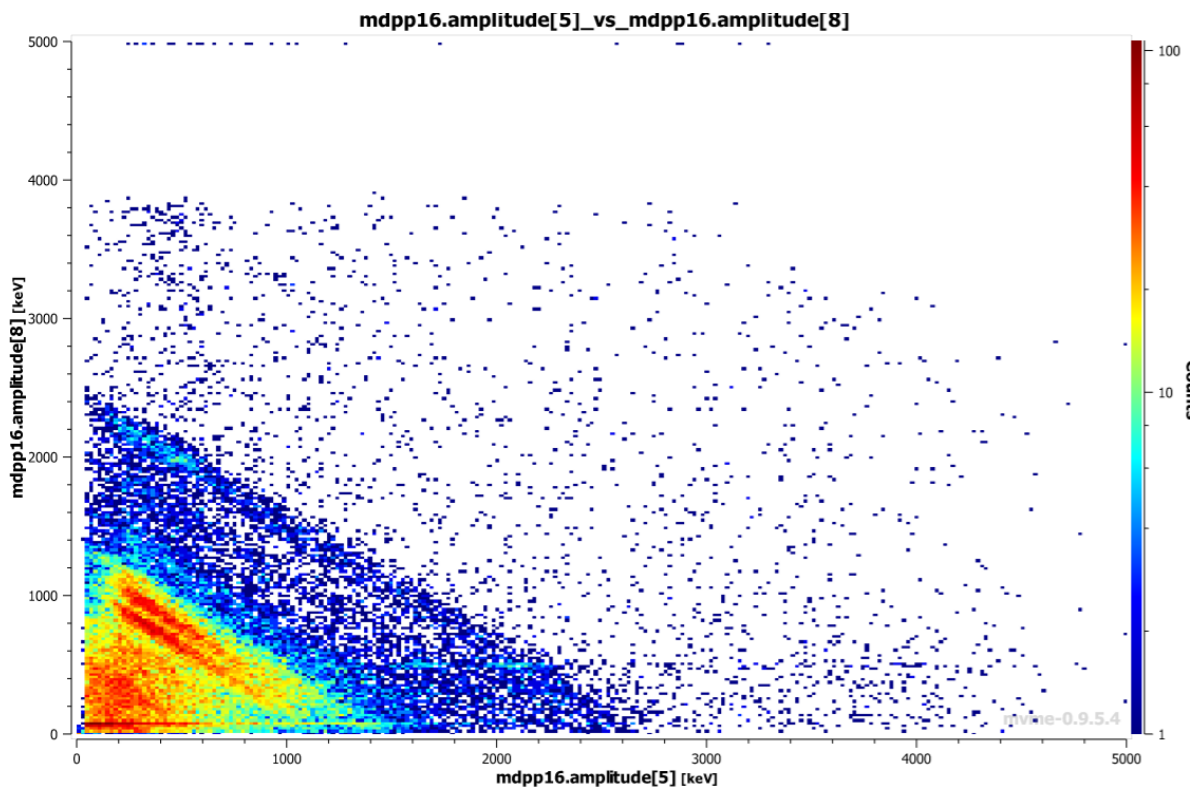
9.3 2D energy spectra for all sources
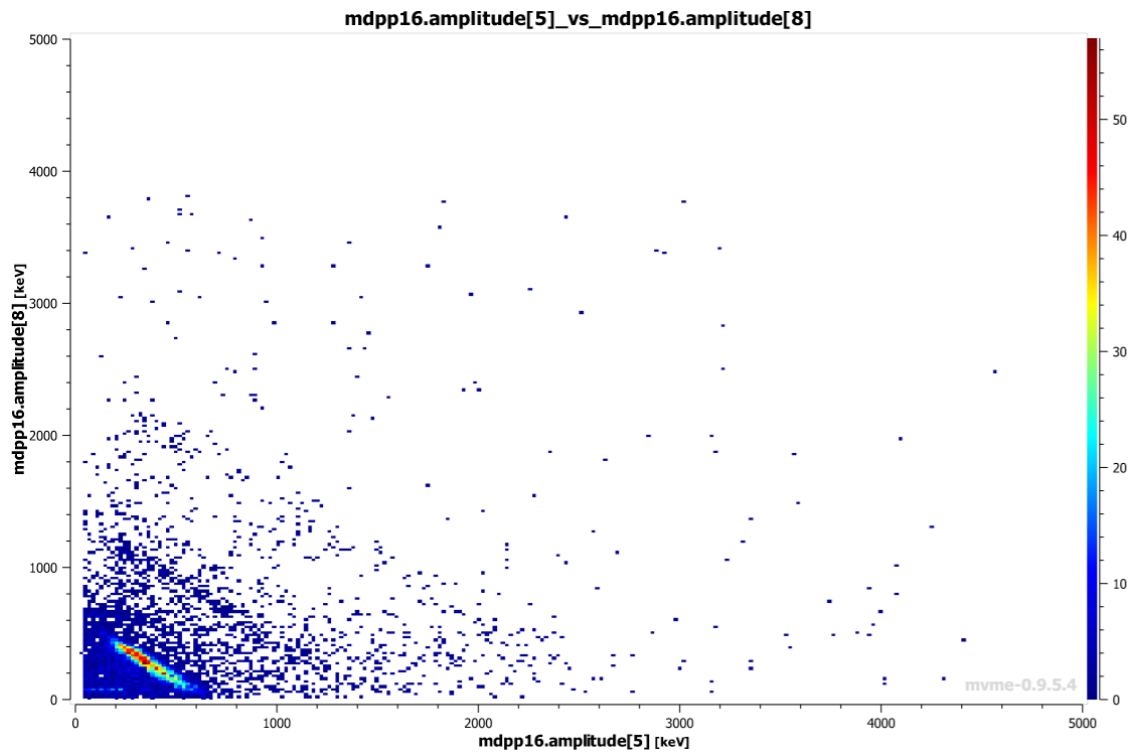
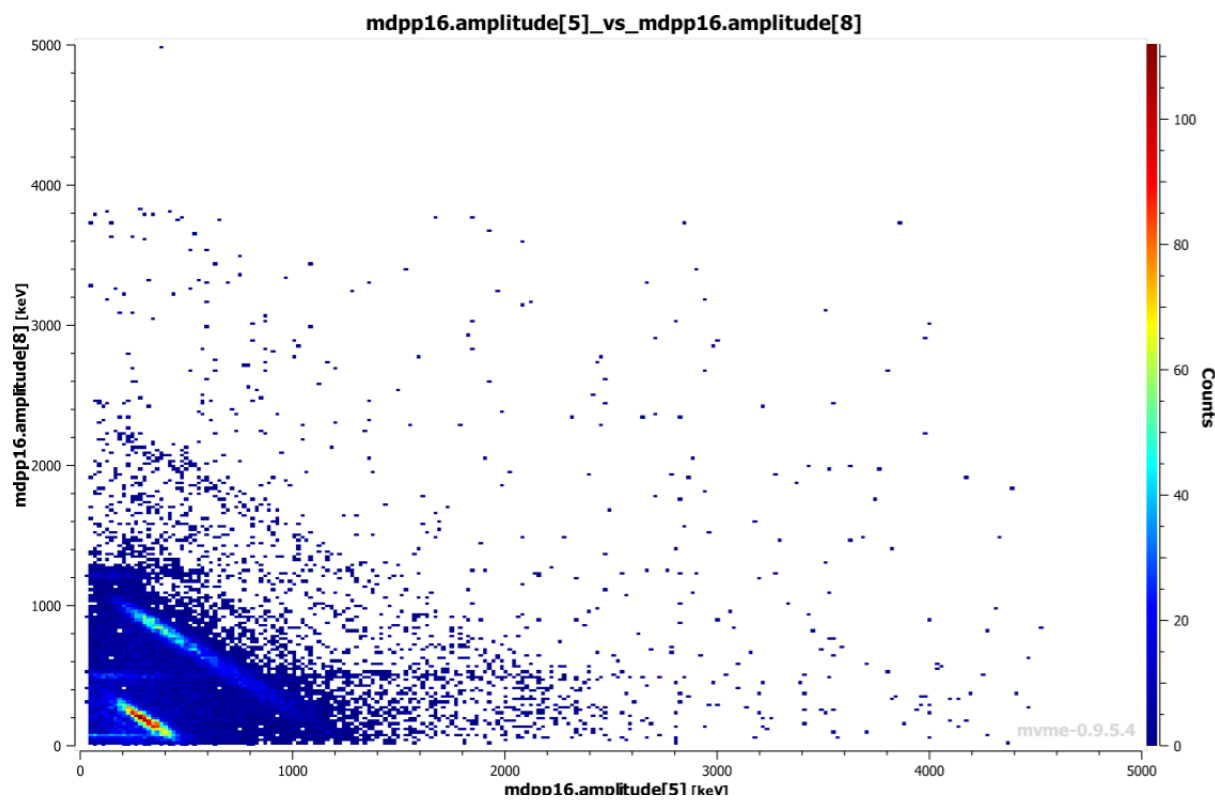^{137}Cs: 158mm away from detector, scale: linear
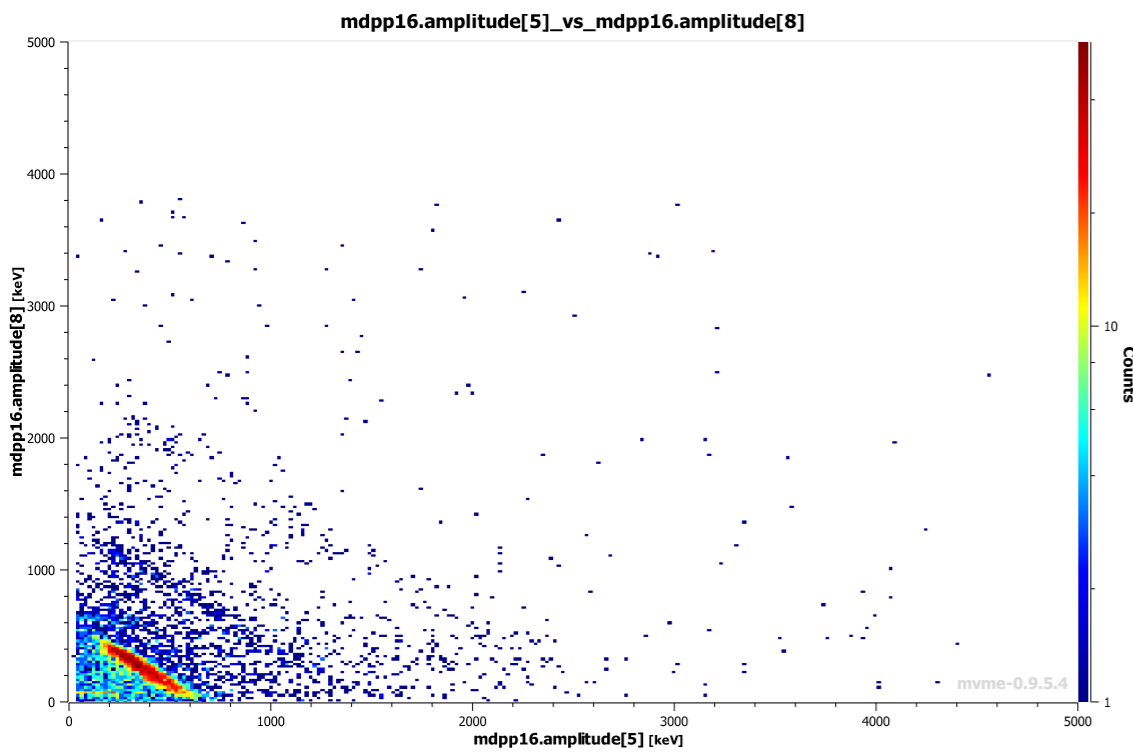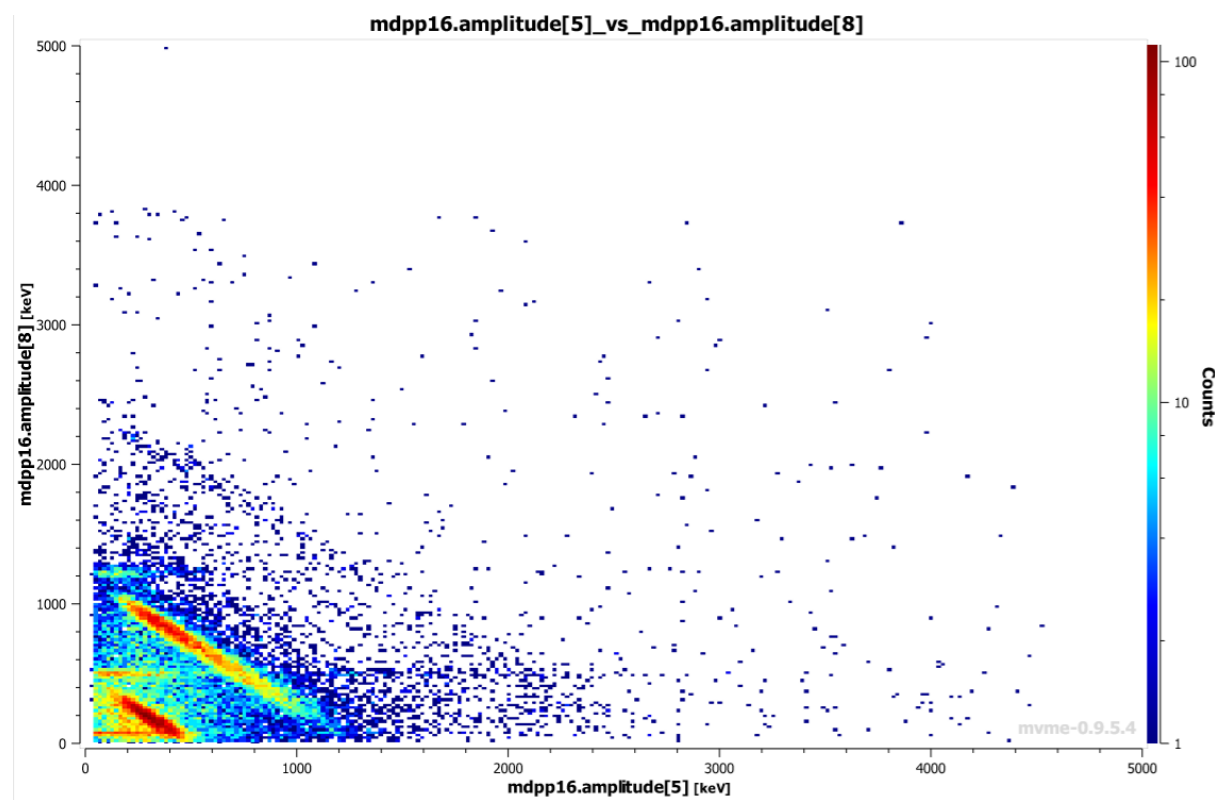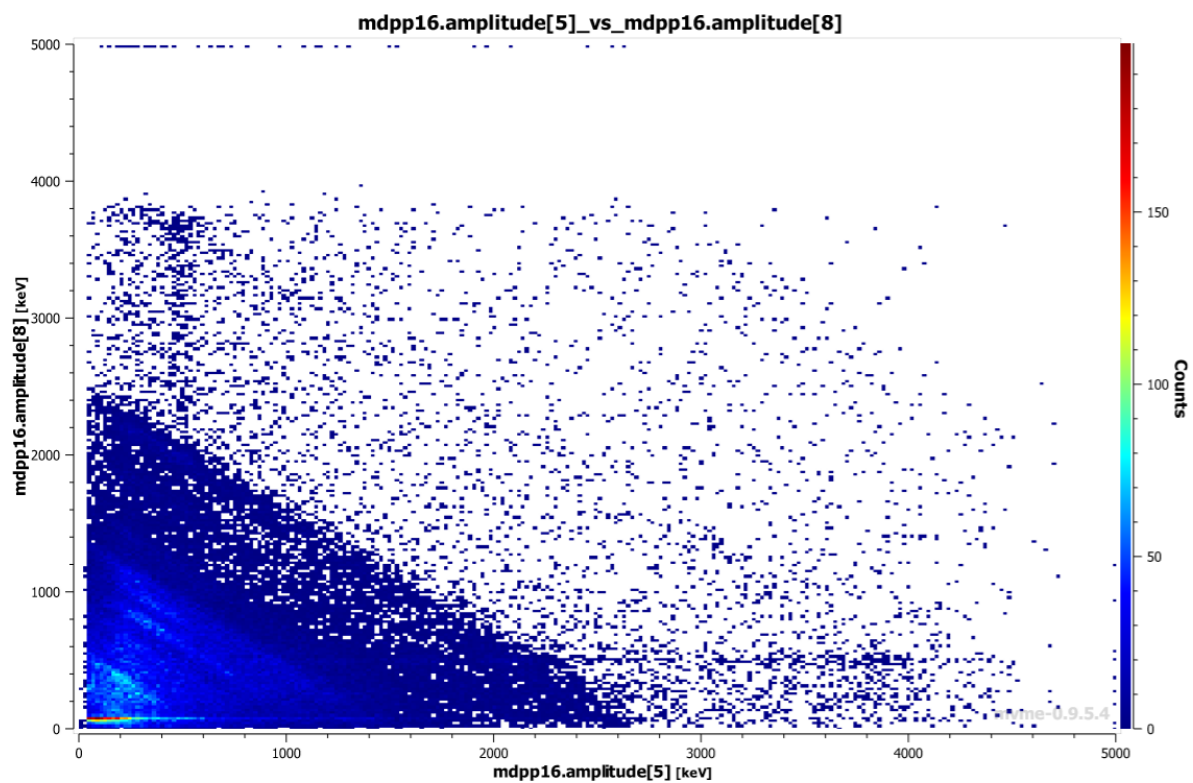

^{137}Cs: 158mm Logarithmic
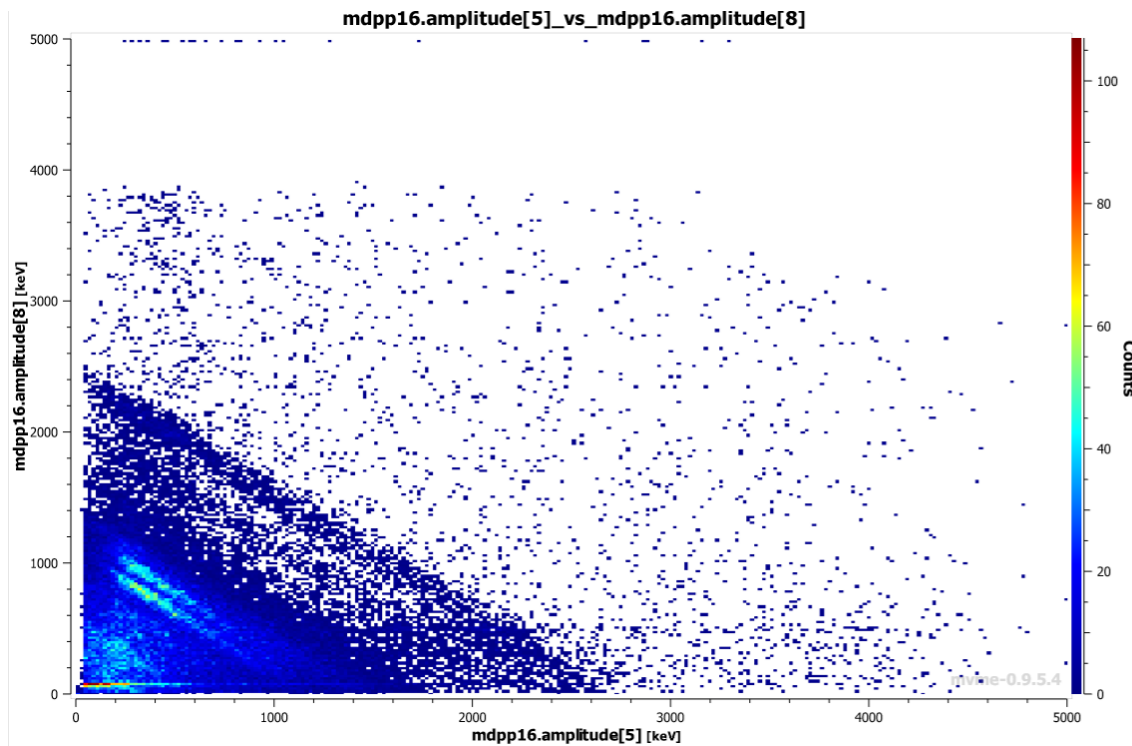
^{60}Co: 158mm linear
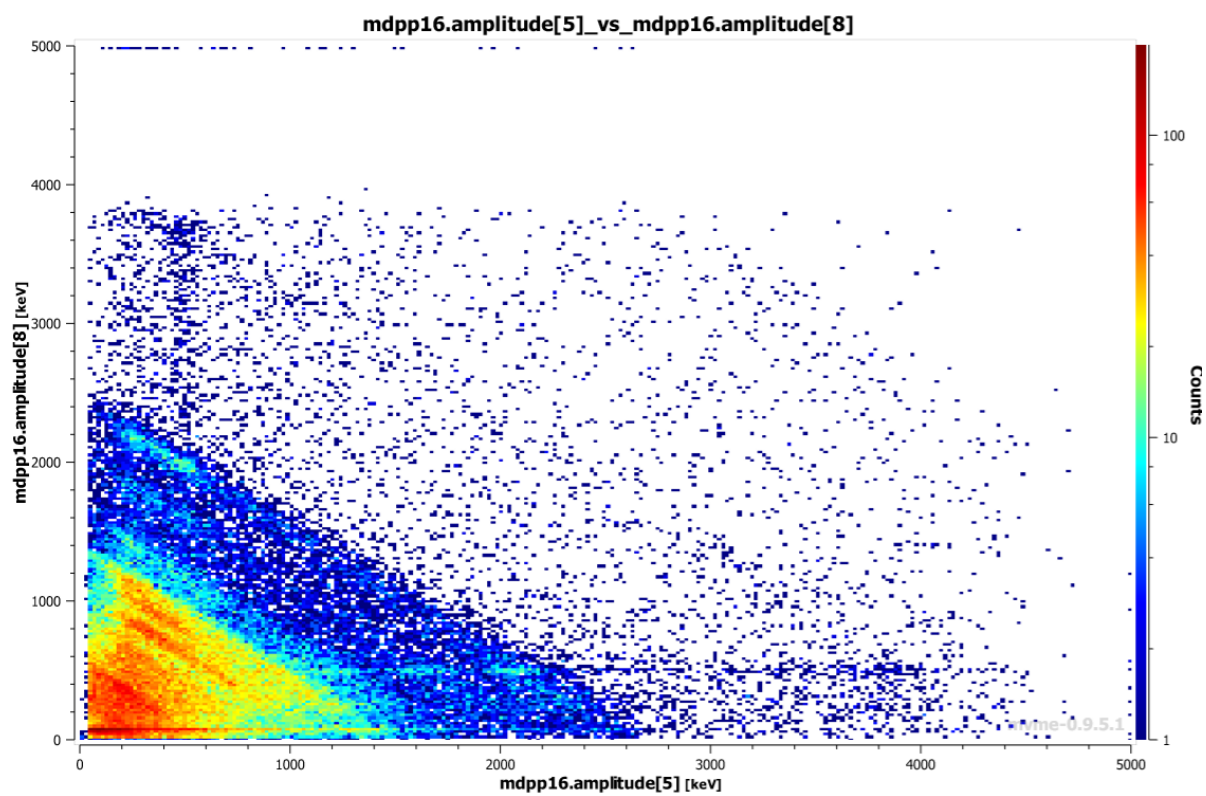

^{60}Co: 158mm logarithmic
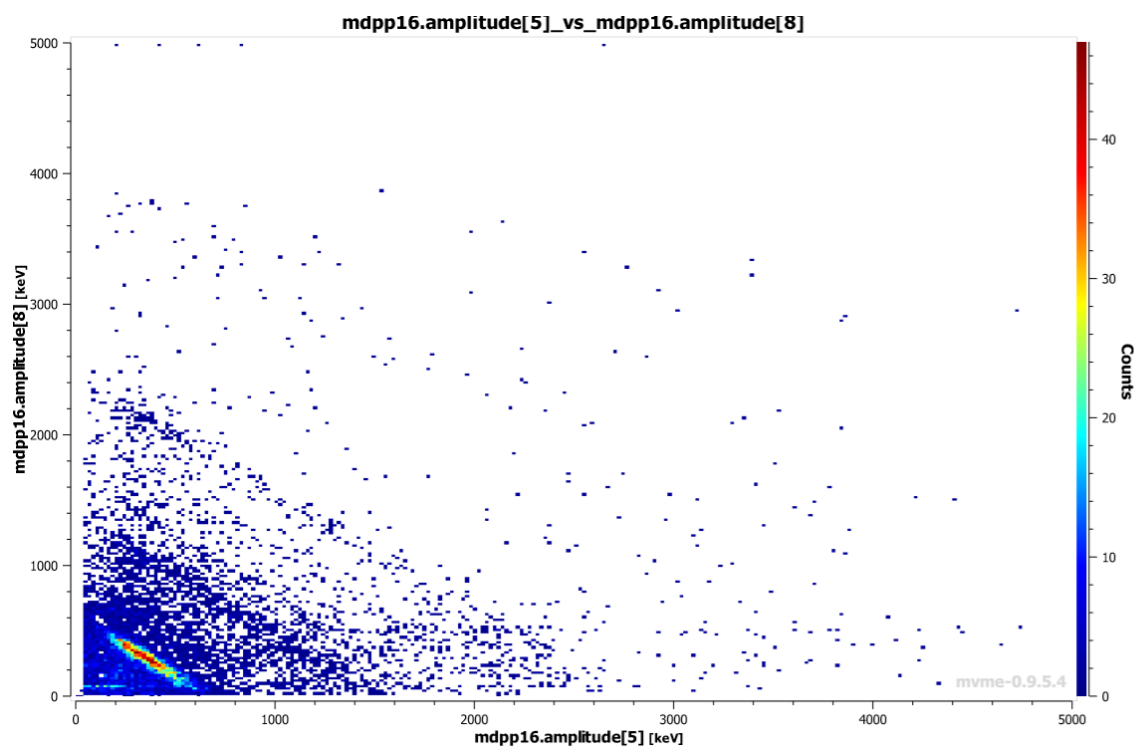
^{22}Na: 250mm linear
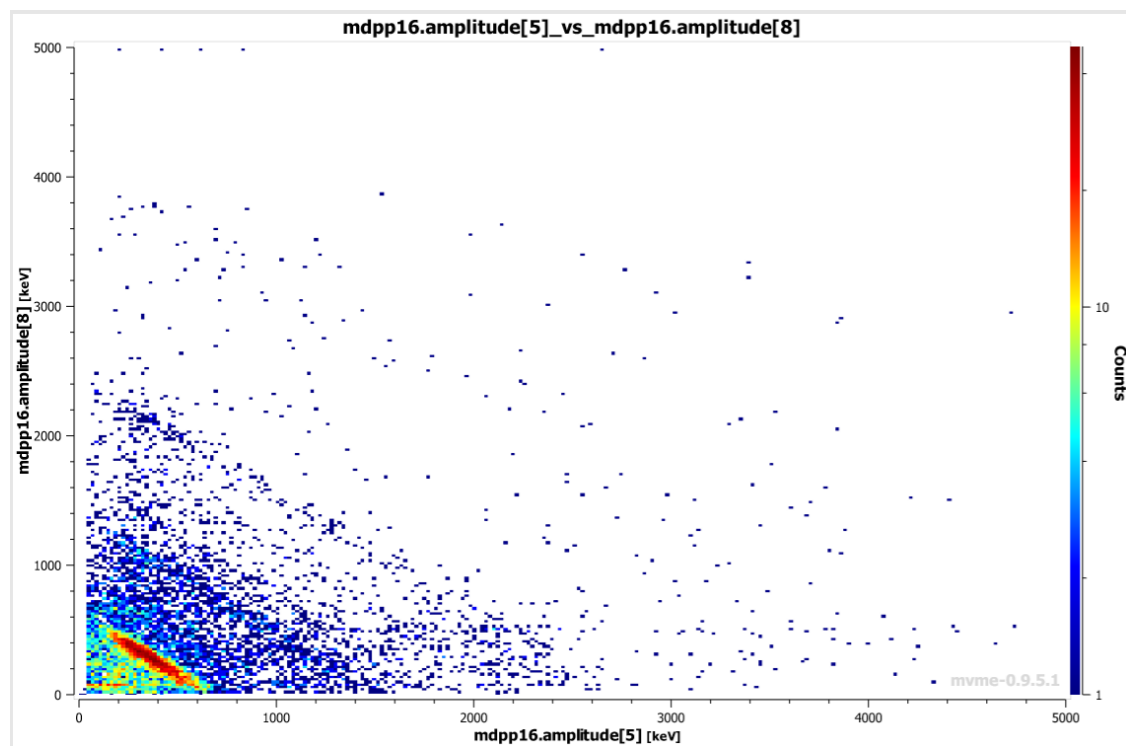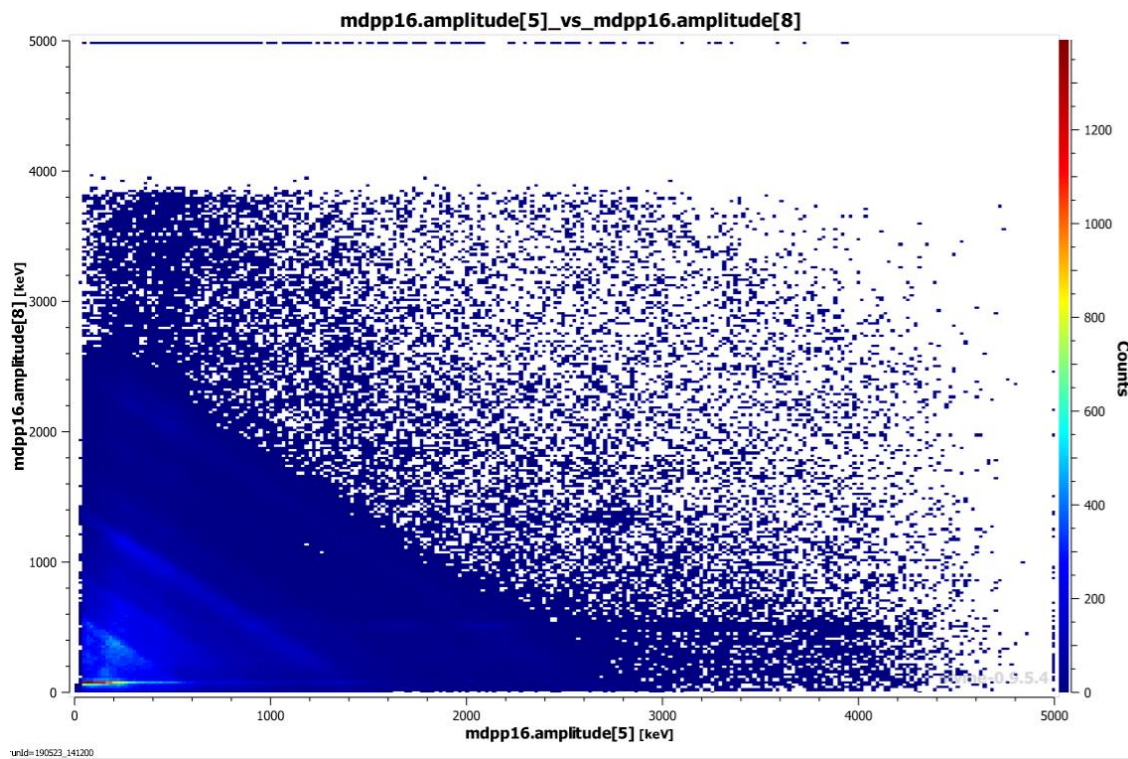

^{22}Na: 250mm logarithmic
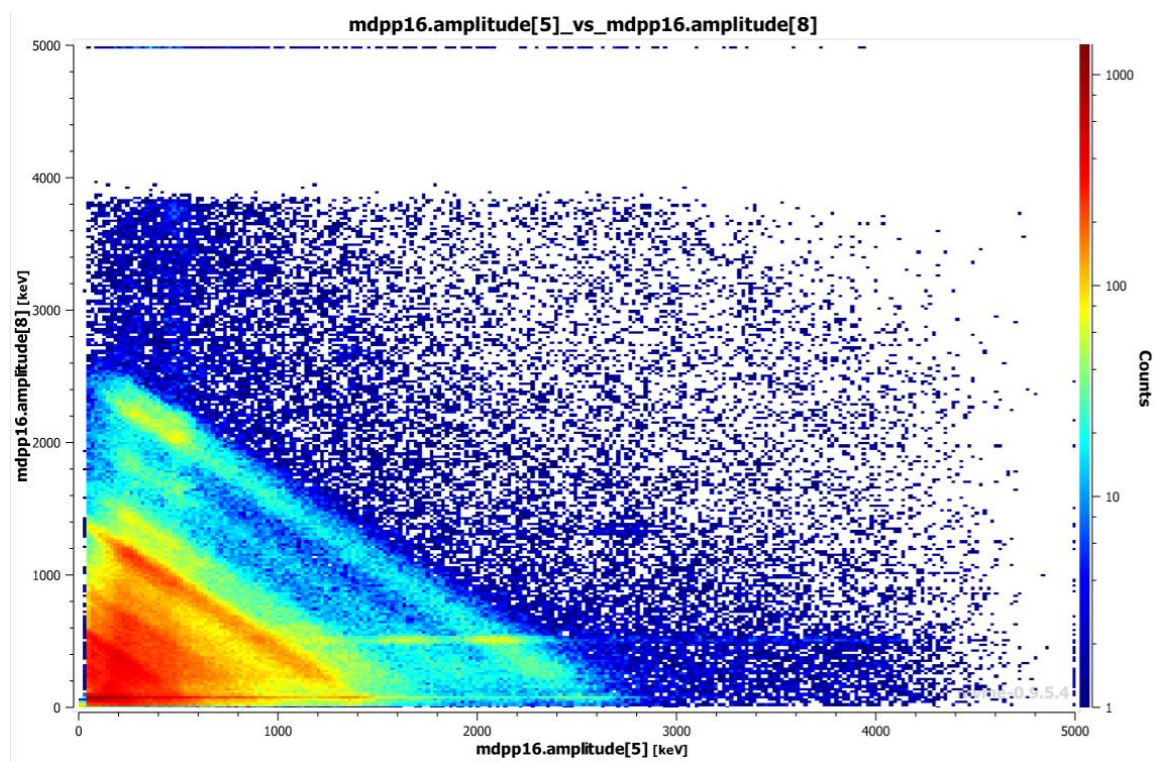
^{60}Co: 250mm linear
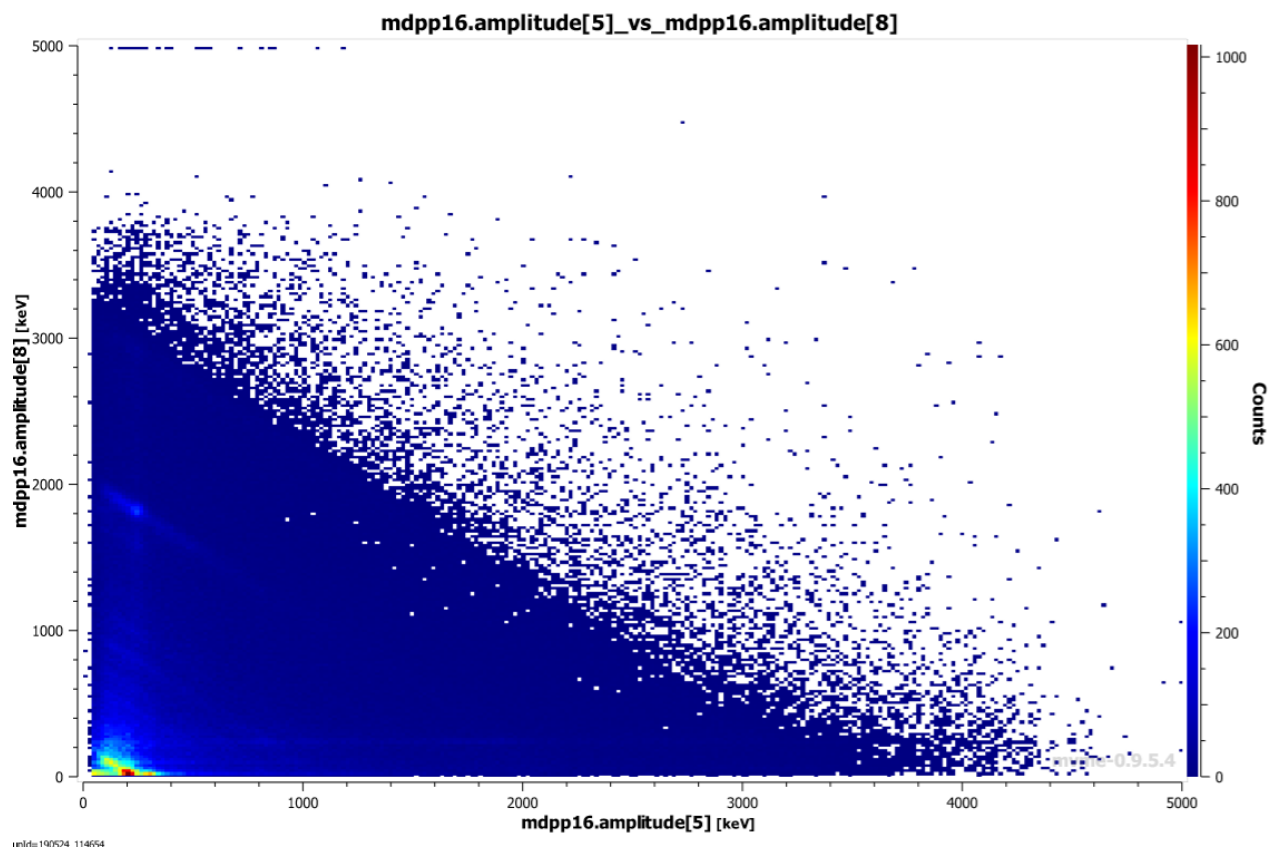

^{60}Co: 158mm logarithmic
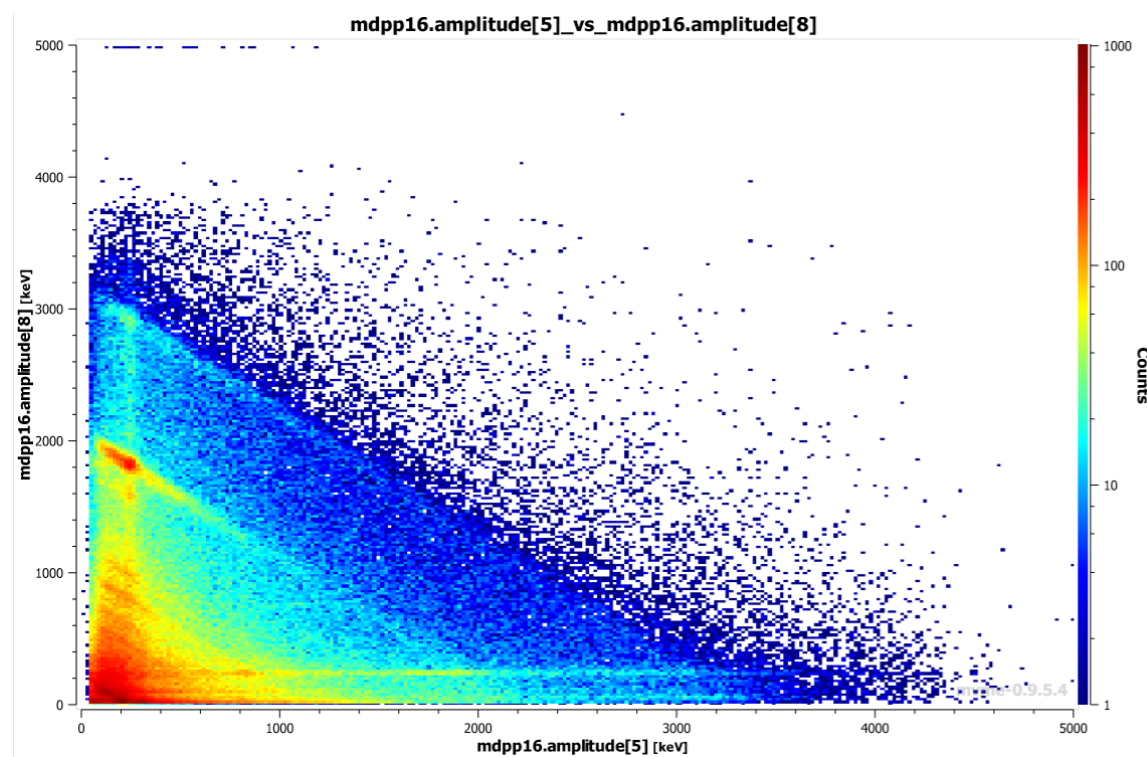
^{137}Cs: 250mm linear
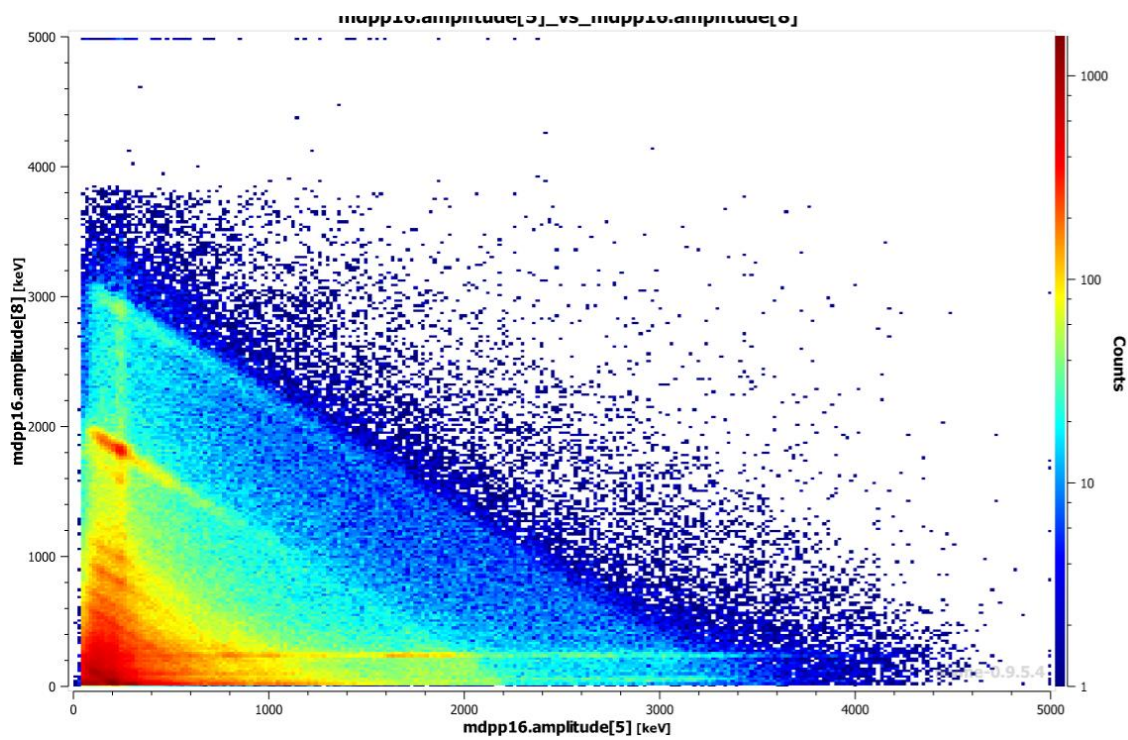

^{137}Cs: 250mm logarithmic
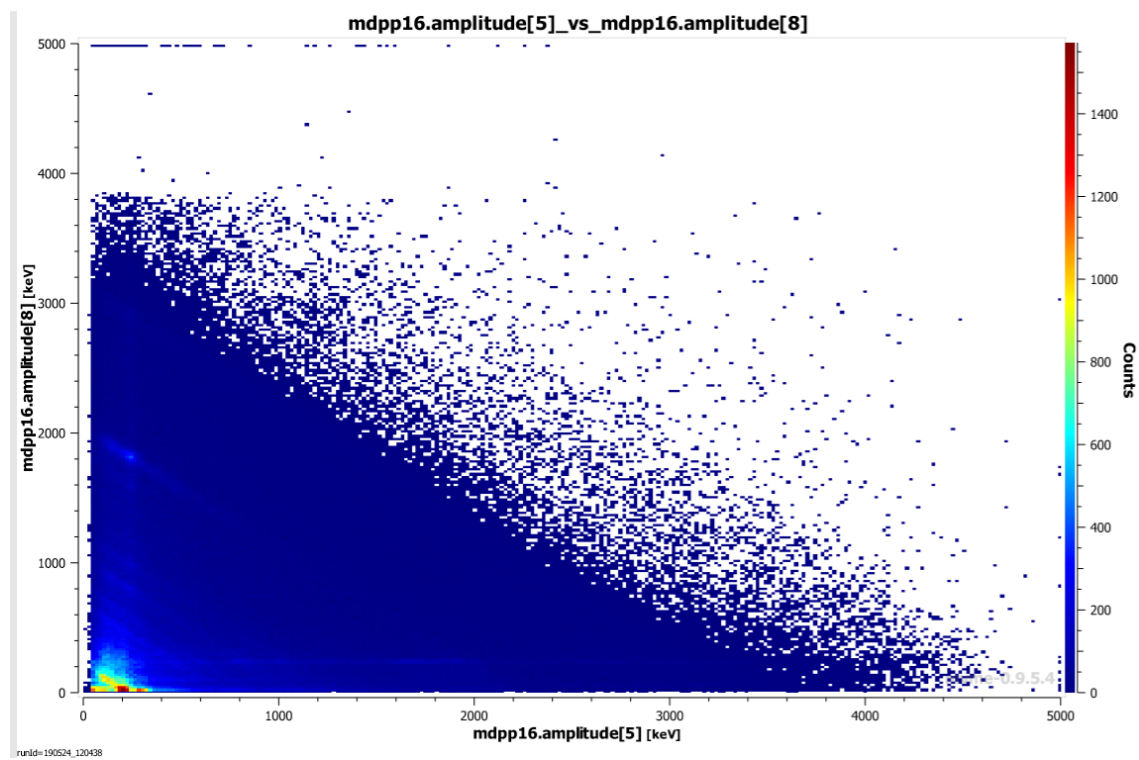
^{24}Na: 0mm linear

^{24}Na: 0mm logarithmic

241Am-Be: 158mm linear

241Am-Be: 158mm logarithmic

²⁴¹Am-Be: 250mm linear

²⁴¹Am-Be: 250mm logarithmic